Politecnico di Torino

Politecnico di Torino

Ingegneria Aerospaziale

A.a. 2025/2026

Sessione di laurea Marzo 2026

Development of a Modular Multi-DOF Motion Simulator for a Pressurized Lunar Rover

Relatori:

Alfonso Pagani
Rodolfo Azzara
Enrico Zappino
Giuseppe Palaia

Candidati:

Aldo Saponaro

Abstract

This thesis presents the development of a motion simulator for a pressurized lunar rover. In the context of long-duration missions, it is of fundamental importance that the locomotion system is designed to ensure both astronaut comfort and vehicle performance in the lunar environment. To ensure this aim, the work presents a preliminary study of the state-of-the-art in rover locomotion systems and an in-depth study of vehicle dynamics in order to correctly integrate the governing equations within the simulator developed in Simulink. Starting from classical terramechanics formulations that dictate the complex wheel-soil interaction mechanism , including Bekker pressure–sinkage theory and Janosi–Hanamoto shear deformation relations, a simplified wheel–soil interaction model based on formulations reported in NASA technical literature was extended to account for combined longitudinal and lateral slip effects and implemented in the simulator. The model was conceived with a modular architecture that allows for changing the number of wheels, the steering system, and the traction system. This flexibility makes it possible to explore different configurations and understand the pros and cons of each layout. In this work, the system has been developed as a modular structure consisting of a 6-DOF main chassis and independent 2-DOF wheel-suspension units. Each wheel-suspension assembly is treated as an independent unit, allowing the possibility to set torque and steering inputs for every single wheel. This approach enabled the exploration of different architectures across various mission operational scenarios. The preliminary results demonstrate the potential of the proposed model to support the development of the locomotion system from the early stages of the design phase.

Contents

List of Figures

Chapter 1

Introduction

1.1 Lunar Rover

A rover is a vehicle designed to operate on the surface of celestial bodies for exploration purposes. A lunar rover is specifically designed to operate on the Moon. Rovers can be classified as *unmanned* (without crew) and *manned* (with crew). The former are remotely controlled vehicles, typically characterized by relatively small dimensions. *Manned* rovers, on the other hand, are designed to transport a crew and can be either pressurized or unpressurized. Manned rovers can be distinguished in pressurized or non pressurized. Pressurized rovers are habitable vehicles that allow astronauts to live inside without wearing a spacesuit. These systems are generally heavier and are intended for long-duration missions.

1.1.1 State of the art for manned rover

Non pressurized

The first example of a non pressurised rover is found in the *Lunar Roving Vehicle* (LRV) 1.1, used by NASA for the Apollo 15, 16 and 17 missions. The LVR was a 4 wheel lightweight electric vehicle designed to operate in the low-gravity vacuum environment of the Moon. It enabled Apollo astronauts to significantly extend the range of their extravehicular activities by traversing the lunar surface.[1] To date, the Lunar Roving Vehicle (LRV) remains the only manned rover ever deployed and operated beyond Earth. A more recent example is given by the Lunar Terrain Vehicle (LTV) concepts developed for NASA's Artemis program by Intuitive Machines, Lunar Outpost, and Venturi Astrolab [2].

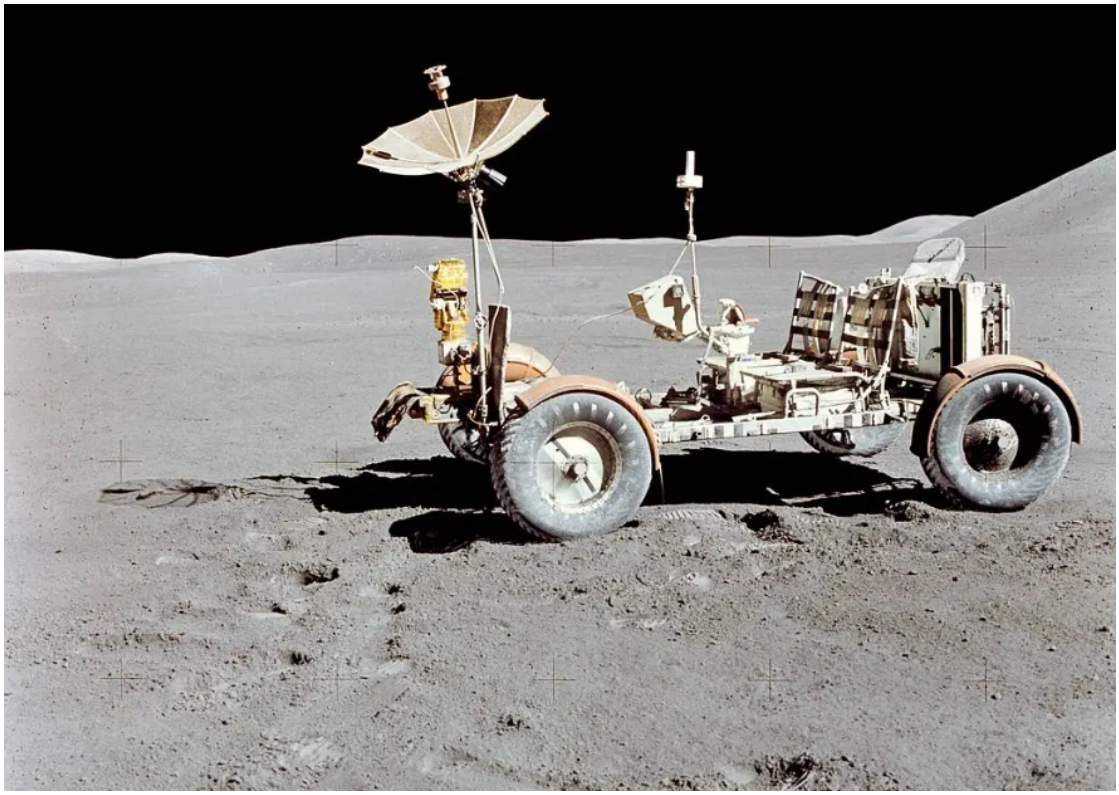

Figure 1.1: Lunar Roving Vehicle on the Moon surface during the Apollo mission[1].

Pressuirized

Pressurized Lunar Rovers represent one of the most advanced solutions for sustained human exploration of the lunar surface. Compared to unpressurized rovers, they combine a pressurized habitable volume with a mobility platform capable of ensuring extended autonomy, enhanced safety, and improved crew comfort during long-duration surface missions. Early pressurized rover concepts were introduced in NASA technical reports from the early 1990s. [3][4] From an engineering standpoint, a pressurized rover can be interpreted as an integrated system in which a mobile habitat with structural, thermal, and safety requirements is combined with a locomotion subsystem encompassing wheels, suspension, and steering.

Suspension Systems

The suspension subsystem plays a fundamental role in both stability and crew comfort. It must isolate the habitable module from terrain-induced vibrations while ensuring continuous wheel–ground contact on uneven lunar regolith. Several

suspension architectures have been investigated for pressurized lunar vehicles. Conventional passive suspensions, derived from automotive layouts such as double wishbone configurations, provide a robust and compact solution suitable for heavy vehicles, allowing control of wheel kinematics and limiting internal mechanical complexity. Alternative concepts, such as rocker–bogie suspensions, are widely adopted in robotic rovers due to their simplicity and obstacle-climbing capability; however, their limited damping performance makes them less suitable for crewed vehicles operating at higher speeds. More advanced solutions include active and semi-active suspensions, capable of adapting stiffness and damping in real time. These systems have been considered for vehicles such as NASA's Space Exploration Vehicle (SEV) [5], enabling improved vibration isolation and allowing the cabin attitude to be actively controlled on inclined terrain.

Steering Systems

Steering design for lunar rovers must balance maneuverability requirements with energy efficiency and terrain preservation. On incoherent regolith, steering maneuvers may generate significant soil disturbance and increased resistive losses. Skid steering represents a mechanically simple option, where vehicle turning is achieved through differential wheel speeds. Nevertheless, this approach can be energetically inefficient and may cause increased wheel sinkage and motor stress. Geometric steering solutions, such as Ackermann steering, reduce lateral slip and energy losses by aligning wheel trajectories toward a common instantaneous center of rotation, although the achievable turning radius may be limited. A further alternative is a double Ackermann steering configuration, in which both the front and rear wheels are steered. Advanced steering architectures include omnidirectional steering, where each wheel can rotate about its vertical axis. This configuration enables crab steering and point turns, which are particularly useful for docking operations or obstacle avoidance. Another viable approach is articulated steering , where the vehicle is divided into two modules connected by a central joint, providing turning capability through relative rotation between modules [3]. Ackermann steering, Skid steering and Articulated frame steering are rapresented in figure1.2

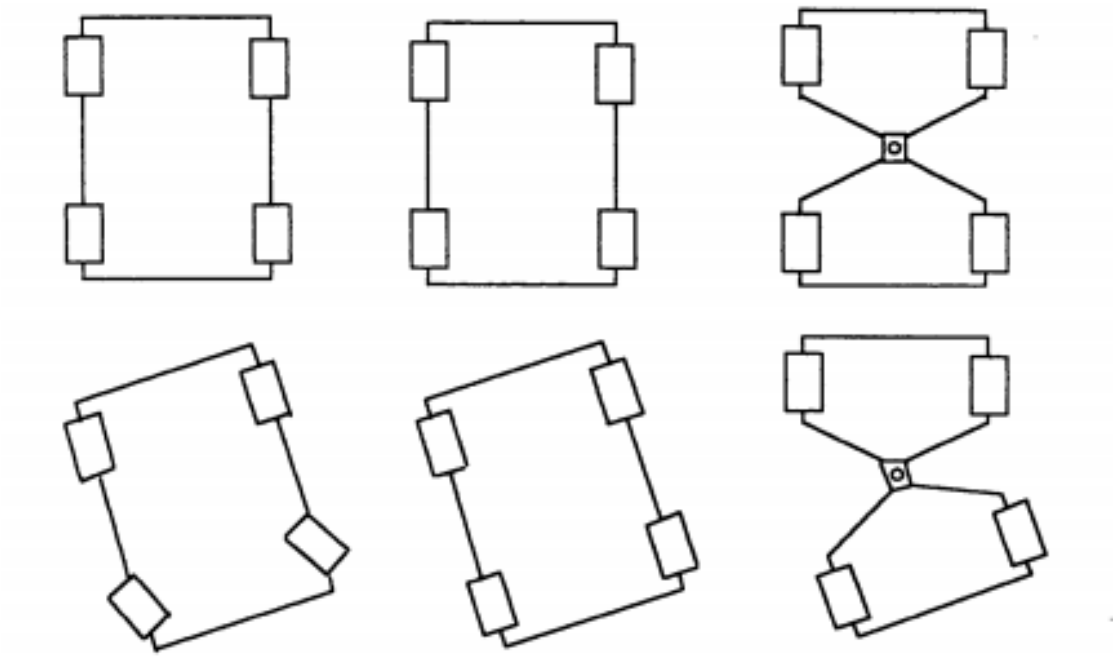

Figure 1.2: Ackermann steering, Skid steering, Articulated frame Steering [3]

Wheel Design

Wheel design represents one of the most critical aspects of planetary mobility. Unlike terrestrial vehicles, lunar rovers cannot rely on pneumatic rubber tires due to the vacuum environment and extreme temperature excursions. Therefore, metallic wheels and compliant structures are typically adopted. Elastic metallic wheels, based on flexible mesh or honeycomb architectures, can provide deformability comparable to that of conventional tires, increasing the contact area and improving traction on regolith. In addition, grousers are commonly integrated as external protrusions designed to penetrate the soil and enhance thrust generation while limiting excessive slip. For heavy pressurized vehicles, wheel diameter and width must be carefully selected to reduce ground pressure and improve obstacle-clearing capability. Typical design solutions for large pressurized rovers require wheel diameters to ensure adequate mobility on uneven terrain.

1.2 Lunar Environment

When designing such a vehicle, it is necessary to take into account the environmental conditions in which it operates. In the lunar environment, the main relevant aspects are the following:

- **Reduced gravity**: Lunar gravity is approximately one sixth of Earth's gravity ($1.62\ \mathrm{m/s^2}$). This results in a lower weight force, which reduces the normal load on the wheels and therefore the traction capability of the vehicle, potentially leading to wheel slip phenomena [6].
- **Extreme temperatures**: Surface temperatures on the Moon are highly variable. They can range from 121 °C down to −246 °C depending on latitude and illumination conditions [7]. Such severe thermal excursions impose strict constraints on materials, sealing systems, and the thermal management of the rover.
- **Regolith**: The lunar surface is covered by a regolith layer several meters thick, composed of fine particles, rock fragments, and dust generated by meteoritic impacts and fracturing processes. The physical and mechanical properties of regolith can lead to sinkage and wheel slip phenomena [8].
- **Radiation**: The lunar surface is exposed to significant levels of ionizing radiation that may be harmful to humans. The main sources include the solar wind, solar energetic particles generated by solar flares, and galactic cosmic rays, mainly composed of protons, neutrons, and heavier nuclei. Since radiation intensity varies with solar activity, a pressurized rover must provide adequate shielding to protect the crew.[3]
- **Micrometeoroids**: Micrometeoroids are small particles (typically below 1 mm in diameter) that represent a hazard on the lunar surface, since they are not stopped by an atmosphere. Impacts of milligram-scale particles may occur roughly once per year, with estimated velocities of 13–18 km/s. Protection can be provided through thin composite shielding or multilayer structures designed to disperse the particle before hull penetration, while critical components should be positioned to reduce exposure to larger, rarer impacts.[3]

1.3 Thesis Objective

The objective of this thesis is to develop a dynamic simulation model for the analysis of the mobility performance of a pressurized lunar rover operating on deformable terrain. The aim of the work is to create a modular simulation framework capable

of integrating vehicle dynamics and wheel–soil interaction models in order to study the influence of rover configuration, steering architecture, and traction system on the overall vehicle behavior. The simulator is designed to provide a flexible tool for investigating different rover layouts and operational scenarios, supporting the preliminary design and analysis of locomotion systems for future lunar exploration missions.

Chapter 2

Vehicle Dynamics

The design of the rover requires a preliminary study of the vehicle dynamics, which includes the vertical dynamics, responsible for the response of the suspension system to terrain irregularities, and the planar dynamics, related to the longitudinal, lateral, and yaw motion. In this chapter, several dynamic vehicle models are introduced, organized according to an increasing level of complexity. The analysis starts from simplified models, useful for the basic study of the suspension system, and progresses to more complete models capable of describing the three-dimensional behavior of the vehicle. The increase in complexity is associated with a higher number of degrees of freedom (DOF) and with a more accurate description of the interactions among the different components of the system. The equations presented in this section are taken from and derived based on the formulations reported in *Vehicle Dynamics and Control* and *Theory of Ground Vehicles*. [9][10]

2.0.1 Rotations Conventions

For the formulation of the dynamic models, the vehicle is considered as a rigid body capable of rotating about its three principal axes. The following conventions are adopted:

- θ: pitch angle, defined as positive for a rotation that lowers the vehicle nose;
- ϕ: roll angle, defined as positive for rotations that raise the left side of the vehicle;
- ψ : yaw angle, defined as positive for clockwise rotations of the veichle around the z axis;

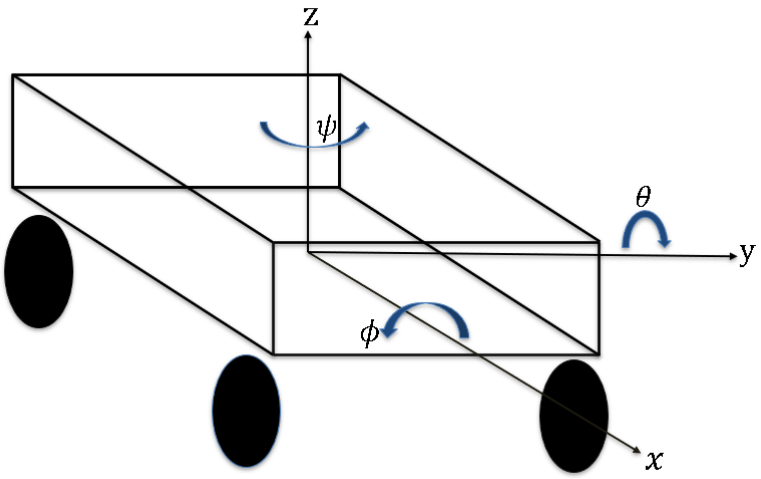

Figure 2.1: Veichle axis and rotations .

2.1 Vertical Vehicle Dynamics

The modeling of the vertical dynamics is aimed at studying the response of the suspension system to the excitations imposed by the terrain profile. In the vehicle model, three main components can be identified:

- **Sprung mass (m_s):** represents the main structure of the rover, including the chassis and onboard systems, and is supported by the suspension system.
- **Unsprung masses (m_u):** include the components downstream of the suspension system, such as wheels, hubs, and in–wheel actuators.
- **Suspension system:** a set of elastic and damping elements connecting the sprung mass to the unsprung masses, with the purpose of isolating the chassis from terrain irregularities.

2.1.1 Variables and Parameters

For the formulation of the models, the following variables and parameters are introduced:

- z_s: vertical displacement of the sprung mass center of gravity;
- z_u: vertical displacement of the unsprung mass;

- z_r: vertical terrain profile (system input);
- k_s, c_s: suspension stiffness and damping coefficient;
- k_t: vertical stiffness of the tire.

2.1.2 Hierarchy of Suspension Dynamic Models

Quarter-Car Model (2 DOF)

The *quarter–car* model represents the simplest configuration of the suspension system and is characterized by two degrees of freedom, z_s and z_u. It consists of a sprung mass, an unsprung mass, and a single suspension system. The wheel is modeled as a linear spring with stiffness k_t, while the suspension is represented by a spring–damper element with coefficients k_s and c_s.

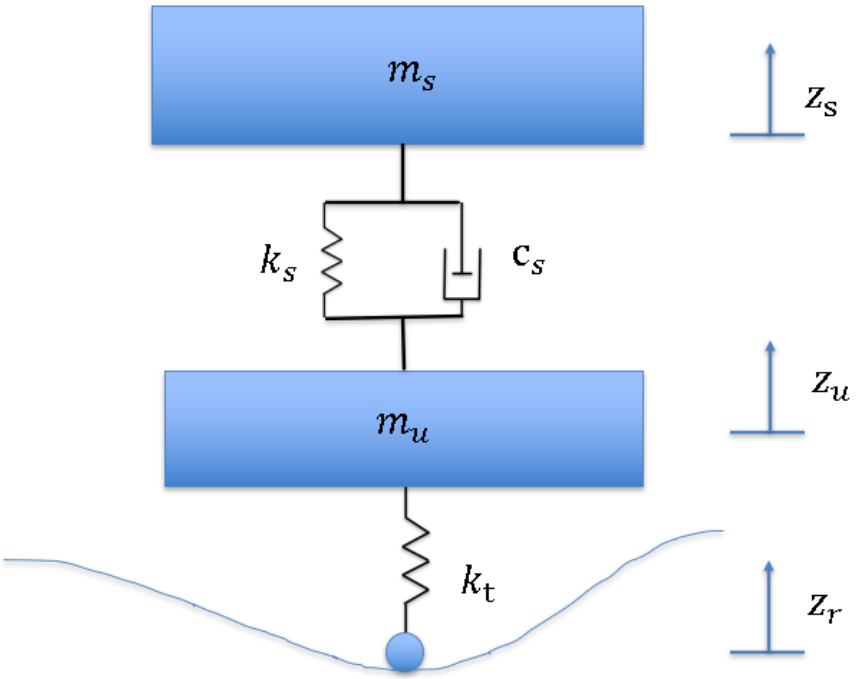

Figure 2.2: 2-DOF quarter car model .

The forces acting on the sprung mass are exclusively due to the suspension:

$$F_{k_s} = -k_s(z_s - z_u), \tag{2.1}$$
$$F_{c_s} = -c_s(\dot{z}_s - \dot{z}_u). \tag{2.2}$$

The elastic force generated by the wheel is:

$$F_t = -k_t(z_u - z_r). \tag{2.3}$$

By applying Newton's second law, the equations of motion are obtained:

- **Sprung mass equilibrium:**

$$m_s\ddot{z}_s + c_s(\dot{z}_s - \dot{z}_u) + k_s(z_s - z_u) = 0, \tag{2.4}$$

- **Unsprung mass equilibrium:**

$$m_u\ddot{z}_u + c_s(\dot{z}_u - \dot{z}_s) + k_s(z_u - z_s) + k_t(z_u - z_r) = 0. \tag{2.5}$$

Half-Car Model (4 DOF)

The *half–car* model extends the quarter–car model by introducing a second unsprung mass, thus allowing the study of the pitch motion of the chassis. The system features four degrees of freedom:

$$(z_s,\ \theta,\ z_{uf},\ z_{ur}).$$

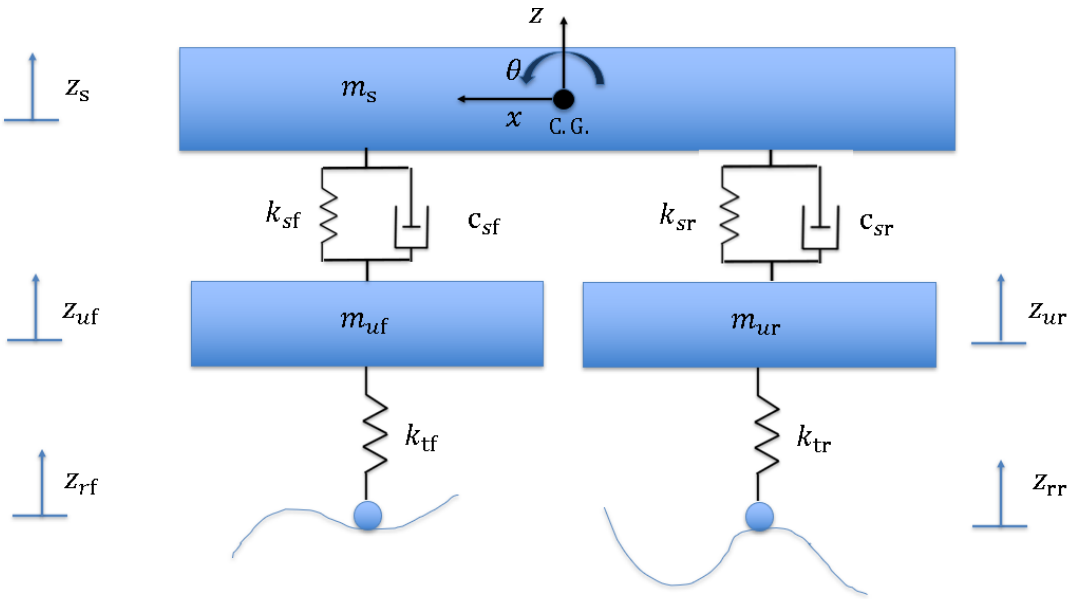

Figure 2.3: 4-DOF half car model.

The front and rear suspension deflections are defined as:

$$\delta_f = z_s - l_f\theta - z_{uf}, \tag{2.6}$$
$$\delta_r = z_s + l_r\theta - z_{ur}, \tag{2.7}$$

where l_f and l_r represent the distances from the vehicle center of gravity to the front and rear wheels, respectively.
The suspension forces are given by:

$$F_{sf} = -k_{sf}\delta_f - c_{sf}\dot{\delta}_f, \tag{2.8}$$
$$F_{sr} = -k_{sr}\delta_r - c_{sr}\dot{\delta}_r. \tag{2.9}$$

The elastic forces acting on the wheels are:

$$F_{tf} = -k_{tf}(z_{uf} - z_{rf}), \tag{2.10}$$
$$F_{tr} = -k_{tr}(z_{ur} - z_{rr}). \tag{2.11}$$

The following equations of motion are obtained:

- **Sprung mass equilibrium:**

$$m_s\ddot{z}_s = F_{sf} + F_{sr} \tag{2.12}$$

- **Sprung mass pitch motion:**

$$I_{yy}\ddot{\theta} = -l_f F_{sf} + l_r F_{sr} \tag{2.13}$$

- **Unsprung masses equilibrium:**

$$m_{uf}\ddot{z}_{uf} = -F_{sf} + F_{tf}, \qquad m_{ur}\ddot{z}_{ur} = -F_{sr} + F_{tr} \tag{2.14}$$

Full-Car Model (7 DOF)

The *full–car* model represents the most complete extension of the vehicle vertical dynamics and allows a three-dimensional description of the motion.

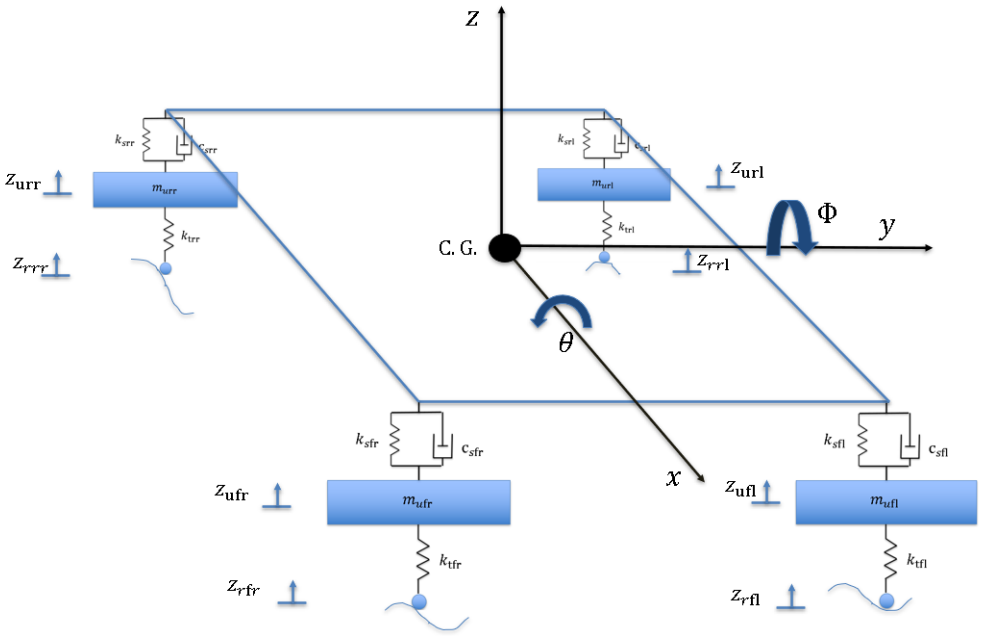

Figure 2.4: 7-DOF vehicle model.

Figure 2.4 shows the full-car model configuration and the adopted conventions for pitch and roll rotations. The system features seven degrees of freedom:

$$(z_s,\ \theta,\ \phi,\ z_{ufl},\ \ z_{ufr},\ \ z_{url},\ \ z_{urr}). \tag{2.15}$$

The vertical displacements of the suspension attachment points on the sprung mass are expressed as:

$$z_{sfl} = z_s - l_f\theta + b_l\phi, \tag{2.16}$$
$$z_{sfr} = z_s - l_f\theta - b_r\phi, \tag{2.17}$$
$$z_{srl} = z_s + l_r\theta + b_l\phi, \tag{2.18}$$
$$z_{srr} = z_s + l_r\theta - b_r\phi. \tag{2.19}$$

where b_l and b_r represent the distances from the center of gravity to the left and right sides of the vehicle, respectively. The suspension forces are defined as:

$$F_{sij} = -k_{sij}(z_{sij} - z_{uij}) - c_{sij}(\dot{z}_{sij} - \dot{z}_{uij}), \tag{2.20}$$

while the wheel elastic forces are:

$$F_{tij} = -k_{tij}(z_{uij} - z_{rij}). \tag{2.21}$$

where the index $ij \in \{fl, fr, rl, rr\}$ identifies the front-left, front-right, rear-left, and rear-right wheels, respectively.
The equations of motion for the sprung mass are:

- **Sprung mass vertical equilibrium:**

$$m_s \ddot{z}_s = \sum_{ij} F_{sij} \tag{2.22}$$

- **Sprung mass pitch motion:**

$$I_{yy} \ddot{\theta} = -l_f (F_{sfl} + F_{sfr}) + l_r (F_{srl} + F_{srr}) \tag{2.23}$$

- **Sprung mass roll motion:**

$$I_{xx} \ddot{\phi} = b_f (F_{sfl} - F_{sfr}) + b_r (F_{srl} - F_{srr}) \tag{2.24}$$

while for each unsprung mass the following relation holds:

$$m_{uij} \ddot{z}_{uij} = -F_{sij} + F_{tij}. \tag{2.25}$$

2.2 Reference Frames

In this section, the reference frames adopted for the study of vehicle dynamics are defined.

Local and Global Reference Frames

First, an inertial reference frame fixed to the ground is defined, denoted as $\mathcal{G} = (X, Y, Z)$, with the Z axis oriented vertically upward. This frame is used to describe the global position and trajectory of the vehicle in the horizontal plane. The position of the vehicle center of gravity in the inertial frame is described by the coordinate vector $\mathbf{r}_{CG} = (X, Y)$. A vehicle-fixed reference frame is then defined, denoted as $\mathcal{B} = (x, y, z)$, with its origin located at the vehicle center of gravity. The x axis is oriented along the longitudinal direction and points toward the front of the vehicle, the y axis is oriented in the lateral direction and points to the left, while the z axis is oriented vertically upward, thus forming a right-handed coordinate system. The vehicle-fixed reference frame $\mathcal{B}$ coincides with the one used in the formulation of the vertical dynamics and suspension models presented in the previous section. The orientation of the frame $\mathcal{B}$ with respect to the inertial frame $\mathcal{G}$ is described by the yaw angle ψ. The longitudinal and lateral velocities of the vehicle, denoted as v_x and v_y, respectively, are expressed in the vehicle-fixed reference frame $\mathcal{B}$. The angle between the longitudinal direction of the vehicle and the direction of the center of mass velocity in the local reference frame is referred to as the *sideslip* angle β. The adopted reference frames configuration is shown in Figure 2.5.

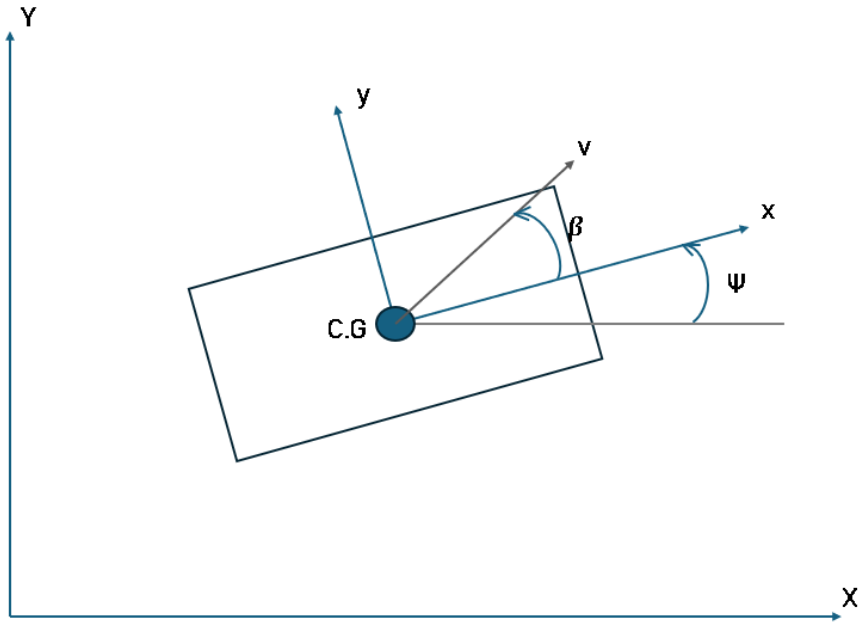

Figure 2.5: Global and vehicle-fixed reference frames, showing the yaw angle ψ and the sideslip angle β.

The rover trajectory in the inertial plane is obtained by integrating the velocities expressed in the global reference frame:

$$\dot{X} = v_x \cos\psi - v_y \sin\psi, \tag{2.26}$$

$$\dot{Y} = v_x \sin\psi + v_y \cos\psi. \tag{2.27}$$

Wheel Reference Frame

For each wheel i, a local reference frame $\mathcal{W}_i$ is defined, fixed to the wheel itself. The axis $x_i^{(w)}$ is oriented along the wheel plane, while the axis $y_i^{(w)}$ is orthogonal to it within the contact plane pointing left.

Figure 2.6: Local wheel reference frame $\mathcal{W}_i$: top view (left) and side view (right) showing internal axes, angular velocity, and acting forces.

The orientation of the frame $\mathcal{W}_i$ with respect to the vehicle reference frame $\mathcal{B}$ is defined by the steering angle δ_i. The angle between the longitudinal direction of the wheel and the velocity vector of the wheel itself is defined as the slip angle α. For a steered wheel, it is defined as:

$$\alpha_i = \delta_i - \theta_v \tag{2.28}$$

where δ_i represents the steering angle of the wheel with respect to the vehicle-fixed reference frame, and θ_v is the angle that the velocity vector makes with the longitudinal axis. The angle θ_v can be expressed in terms of the center-of-gravity velocities and the yaw rate in the vehicle-fixed reference frame, knowing the position of the tire with respect to the vehicle reference frame.

$$\alpha_i = \delta_i - \arctan\left(\frac{v_y + x_i\dot{\psi}}{v_x - y_i\dot{\psi}}\right) \tag{2.29}$$

The terms inside the brackets represent the local velocities at the wheel hub, accounting for the vehicle's rigid body motion:

$$v_{yt} = v_y + x_i\dot{\psi} \tag{2.30}$$

Lateral velocity in the vehicle reference frame at the i-th wheel location.

$$v_{xt} = v_x - y_i\dot{\psi} \tag{2.31}$$

Longitudinal velocity in the vehicle reference frame at the i-th wheel location.

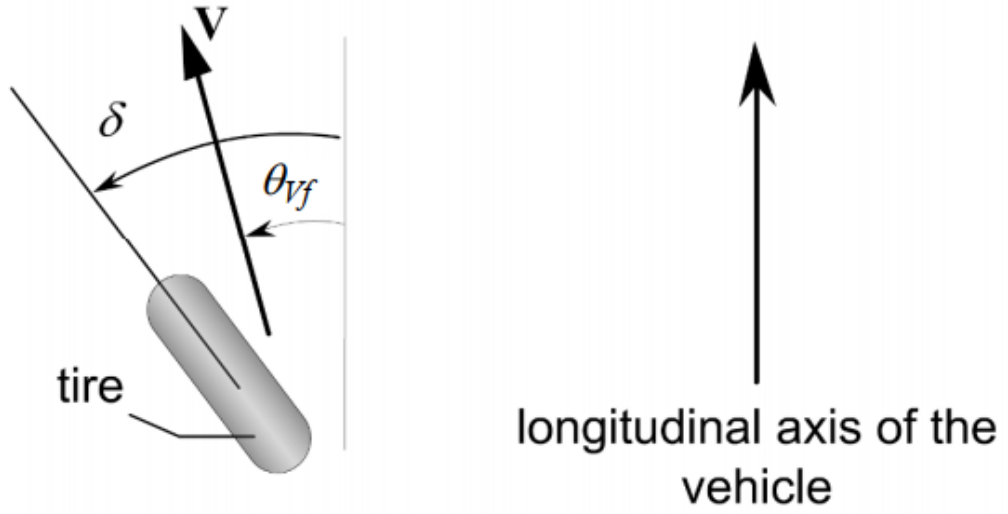

Figure 2.7: Steering tire and slip angle

[9]

If the wheel is not subject to any steering angle, the equation becomes:

$$\alpha_i = -\arctan\left(\frac{v_y + x_i\dot{\psi}}{v_x - y_i\dot{\psi}}\right). \tag{2.32}$$

2.3 Planar Vehicle Dynamics

The vehicle dynamics is modeled by considering a rigid body with three degrees of freedom in the horizontal plane:

- v_x: velocity along the longitudinal axis;
- v_y: velocity along the lateral axis;
- ψ: yaw angle, which defines the rotation about the vertical z axis.

In order to correctly describe the motion in a vehicle-fixed (non-inertial) reference frame, the inertial accelerations at the center of mass must be defined by including the transport and centripetal terms:

$$a_x = \dot{v}_x - v_y\dot{\psi} \tag{2.33}$$

$$a_y = \dot{v}_y + v_x\dot{\psi} \tag{2.34}$$

2.3.1 Longitudinal Dynamics

A vehicle moving on a road with a slope angle θ is considered. Neglecting aerodynamic drag forces, the external longitudinal forces acting on the vehicle include the tire longitudinal forces and the rolling resistance forces. The governing equation is:

$$ma_x = \sum F_{x,i} \; - \sum R_{x,i} \; - mg\sin(\theta) \tag{2.35}$$

where:

- $F_{x,i}$ are the components of the forces applied at the wheels along the longitudinal direction of the vehicle;
- $R_{x,i}$ are the rolling resistance forces acting along the longitudinal direction;
- $mg\sin(\theta)$ is the component of the gravitational force opposing the longitudinal acceleration.

Substituting the expression of a_x from Eq. 2.33 yields:

$$\dot{v}_x = \frac{1}{m}\left(\sum_i F_{x,i} - \sum_i R_{x,i} - mg\sin(\theta)\right) + v_y\dot{\psi}. \tag{2.36}$$

2.3.2 Lateral Dynamics

The lateral translational motion equation is governed by the balance of the lateral forces $F_{y,i}$ generated by the i-th wheel in the vehicle reference frame:

$$ma_y = \sum_i F_{y,i} \tag{2.37}$$

Substituting the definition of a_y from eq. (2.34), the expression for the derivative of the lateral velocity is obtained:

$$\dot{v}_y = \frac{1}{m}\left(\sum_i F_{y,i}\right) - v_x\dot{\psi} \tag{2.38}$$

2.3.3 Wheel–Vehicle Force Transformation

The forces introduced so far are the components of the wheel forces projected in the vehicle reference frame. The forces computed in the wheel reference frame are rotated into the vehicle-fixed reference frame according to the steering angle δ_i:

$$\begin{bmatrix} F_{x,i} \\ F_{y,i} \end{bmatrix} = \begin{bmatrix} \cos\delta_i & -\sin\delta_i \\ \sin\delta_i & \cos\delta_i \end{bmatrix} \begin{bmatrix} F_{x,i}^{(w)} \\ F_{y,i}^{(w)} \end{bmatrix}. \tag{2.39}$$

If the steering angle is zero, the force components reduce to:

- $F_{x,i} = F_{x,i}^{(w)}$
- $F_{y,i} = F_{y,i}^{(w)}$

2.3.4 Yaw Dynamics

The rotation of the vehicle about the vertical axis is produced by the resultant moment of the longitudinal and lateral forces computed with respect to the center of gravity. According to the adopted reference frame convention, a positive contribution to yaw is generated by forces that tend to rotate the vehicle counterclockwise about the z axis. In particular, the front lateral forces and the longitudinal forces applied on the right side of the vehicle provide a positive contribution, whereas the rear lateral forces and the longitudinal forces applied on the left side provide a negative contribution. The yaw moment balance equation, expressed through the characteristic lever arms of the vehicle, can be written as:

$$I_{zz}\ddot{\psi} = \sum l_f F_{y,f} - \sum l_r F_{y,r} + \sum b_r F_{x,r} - \sum b_l F_{x,l} \tag{2.40}$$

where I_{zz} is the vehicle moment of inertia about the vertical axis.

2.4 Sprung Mass Roll Dynamics

For the analysis of lateral load transfer, the rover is modeled as a sprung mass with a single degree of freedom associated with the roll angle ϕ, illustrated in Figure2.8. In this formulation, the mass of the wheels and axles (unsprung masses) is assumed to be negligible with respect to the chassis, and the vehicle is assumed to travel on a flat surface with zero *bank* angle.
While the quarter-car and full-car models introduced in the previous sections describe the vehicle dynamics with respect to the center of gravity, the present formulation follows a reduced-order sprung mass model in which the roll motion is described about the roll center.
Let I_{xx} be the roll moment of inertia about the center of gravity, and let h_R be the distance between the center of gravity and the roll center O. Since the roll motion is now described as a rotation about the roll center, the effective rotational inertia about this axis is obtained using the parallel axis theorem, resulting in $(I_{xx} + m_s h_R^2)$. Under the action of a lateral acceleration a_y, the moment balance about the roll center O can be derived by applying d'Alembert's principle.

Roll is defined as positive for rotations that tend to raise the left side of the vehicle. Therefore, the suspension forces acting on the left side provide a positive moment contribution, whereas the suspension forces on the right side provide a negative

contribution. Assuming that the suspension forces act perpendicularly to the sprung mass, the dynamic equation can be written as:

$$(I_{xx} + m_s h_R^2)\ddot{\phi} = m_s a_y h_R \cos\phi + m_s g h_R \sin\phi + \sum b_l F_{sl} - \sum b_r F_{sr} \qquad (2.41)$$

where:

- $m_s a_y h_R \cos\phi$ is the contribution of the inertial lateral acceleration to the roll motion. It is positive since a positive lateral acceleration tends to generate a positive rotation about the roll axis (a centripetal acceleration toward the left tends to lift the left side of the vehicle);
- $m_s g h_R \sin\phi$ is the contribution of the gravitational force applied at the center of mass, which tends to increase the roll angle;
- $\sum b_l F_{sl} - \sum b_r F_{sr}$ is the contribution of the suspension forces.

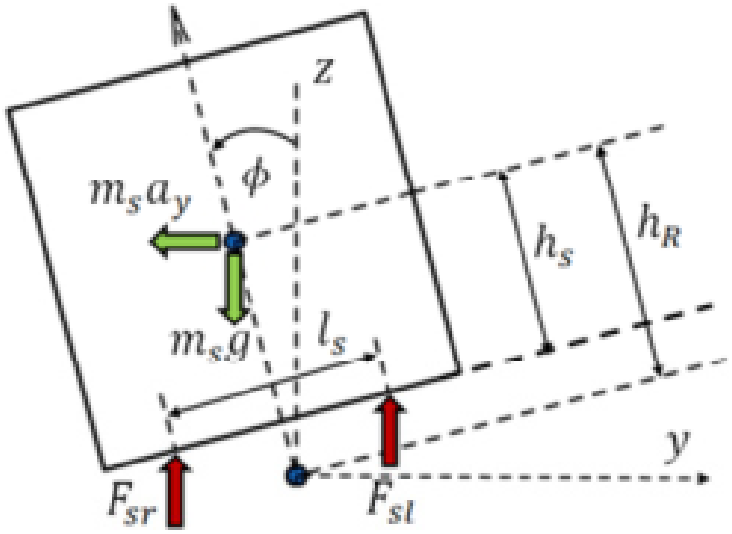

Figure 2.8: Sprung mass roll dynamics.

[9]

2.5 Sprung Mass Pitch Dynamics

The same considerations discussed in the previous subsection apply to the pitch motion. Pitch is defined as positive for rotations that lower the front part of the

vehicle. Therefore, suspension forces acting behind the center of gravity provide a positive contribution to pitch, whereas suspension forces acting ahead of the center of gravity provide a negative contribution. Let h_P be the vertical distance between the center of gravity of the sprung mass and the pitch center, under the action of a longitudinal acceleration a_x, the pitch moment balance equation becomes:

$$(I_{yy} + m_s h_P^2)\ddot{\theta} = -m_s a_x h_P \cos\theta + m_s g h_P \sin\theta + \sum l_r F_{sr} - \sum l_f F_{sf} \tag{2.42}$$

where:

- $-m_s a_x h_P \cos\theta$ is the contribution of the inertial longitudinal acceleration to the pitch motion. It is negative since a positive forward acceleration tends to generate a negative rotation about the pitch axis (a forward acceleration tends to lift the front part of the vehicle);
- $m_s g h_P \sin\theta$ is the contribution of the gravitational force applied at the center of mass, which tends to increase the pitch angle;
- $\sum l_r F_{sr} - \sum l_f F_{sf}$ is the contribution of the suspension forces.

2.6 Vertical Wheel Load

The load transfer between the right and left sides of the vehicle, as well as between the front and rear axles, is a direct consequence of the roll and pitch dynamics. The vertical wheel loads F_{zi} can be expressed as the sum of a static contribution and a dynamic contribution:

$$F_{zi} = \frac{m_s g}{N} + m_u g + F_{ti} \tag{2.43}$$

where the first two terms represent the static load distribution due to the sprung and unsprung masses, while F_{ti} accounts for the additional dynamic contribution related to the wheel vertical stiffness.
These instantaneous vertical loads represent a key input for the wheel–terrain interaction model, since they directly affect the sinkage z and, consequently, the motion resistance and the traction capability of the rover.

2.7 Single Wheel Dynamics

The wheel dynamics is modeled only in the rotation plane. Each wheel is modeled as a rigid body with rotational inertia J_w. The rotational dynamics of the i-th wheel is described by the torque balance:

$$J_w \dot{\omega}_i = T_i - r_w F_{x,i}^{(w)} \tag{2.44}$$

where T_i is the torque applied by the traction system and r_w is the wheel radius.

Chapter 3

Wheel-soil interaction model

In this chapter, the terramechanical model used to simulate the wheel-soil interaction is presented. This model is an extension for lateral forces of a simplified model proposed in the literature to take into account the development of lateral forces.

3.1 Pressure-sinkage relations

The sinkage of the wheel into the lunar terrain is the first step in calculating the generation of forces and resistances. Sinkage is caused by two mechanisms: one static and the other dynamic. Static sinkage is produced by the vertical load to which the wheel is subjected. Dynamic sinkage, on the other hand, is due to the slip ratio [11]. In this discussion, the dynamic component of the sinkage is neglected. The static component of sinkage is given by the equation formulated by Bekker, which describes the vertical pressure exerted on the wheel-soil contact surface as a function of the sinkage z:

$$p = \left(\frac{k_c}{b} + k_\phi \right) z^n \tag{3.1}$$

Where:

- p is the normal pressure at the wheel-soil interface;
- z represents the vertical sinkage;
- b represents the width of the wheel;
- k_c is the cohesive modulus of the terrain;
- k_ϕ is the internal friction modulus of the terrain;
- n is the exponent of soil compaction.

The sinkage z is related to the vertical load by the following formula:

$$z = \left[\frac{3W}{(3-n)\,(k_c + k_\phi b)\,\sqrt{D}} \right]^{\frac{2}{2n+1}} \tag{3.2}$$

Where:

- W is the vertical load acting on the wheel;
- D is the wheel diameter.

Bekker's formula 3.1 is based on the fundamental assumption of a uniform pressure distribution. This approach implies that the penetration of a wheel into the soil can be accurately approximated by the penetration of a flat, rigid plate [11] as can be seen in figure3.1.

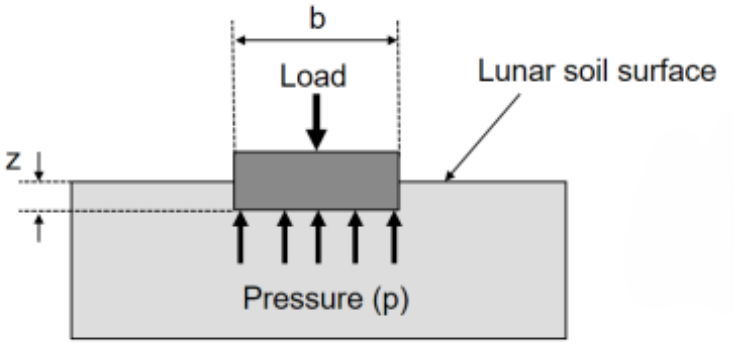

Figure 3.1: Uniform pressure on flate plate

[11]

In reality, the pressure distribution has a trend that can be approximated by a parabola along the contact arc.

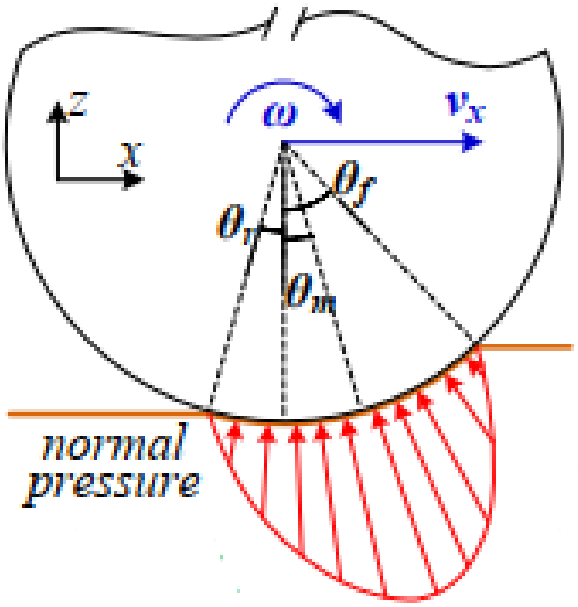

Figure 3.2: Parabolic pressure distribution along the wheel-soil contact arc. [12]

Contact patch geometry

Once the sinkage is obtained, the entry angle and the length of the contact region can be derived through simple trigonometric relations:

$$\begin{aligned} \theta_f &= \cos^{-1}\left(1 - \frac{z}{r}\right) \\ l &= r\theta_f \end{aligned} \tag{3.3}$$

The contact area is therefore defined as:

$$A = bl \tag{3.4}$$

In reality, the contact arc between the soil and the wheel is determined by two angles: the front entry angle θ_f, and the exit angle θ_r due to the elastic recovery of the soil after the wheel passes. In this work, this effect is neglected, thus considering θ_r to be zero.

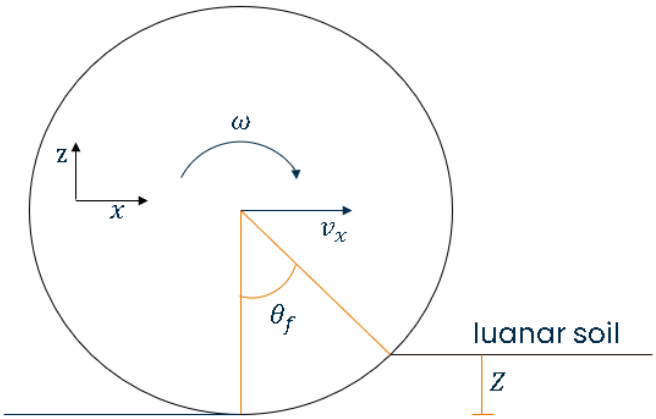

Figure 3.3: Geometric representation of static sinkage z into the lunar regolith and the entry angle θ_f

3.2 Shear-stress generation

The generation of tractive forces on deformable terrain is closely linked to the shear strength of the soil. Specifically, the terrain can sustain tangential stresses only up to a limit value, beyond which material failure occurs, leading to soil yielding. The failure condition can be described using the Mohr-Coulomb criterion, which relates the maximum developable shear stress to the normal pressure acting on the ground. According to this criterion, the maximum allowable shear stress is defined as:

$$\tau_{\max} = c + p\tan(\phi) \tag{3.5}$$

Where:

- c represents the soil cohesion;
- p is the normal pressure acting at the wheel–soil interface;
- ϕ is the internal friction angle of the soil.

This relationship provides the upper limit of the tangential stress developable within the contact zone and is fundamental for calculating the longitudinal and lateral forces generated by the wheel.

Slip Ratio

The longitudinal slip is defined as the difference between the tangential velocity of the wheel, $r\omega$, and its actual longitudinal velocity at the axle, v_x. This quantity

represents the difference between the wheel's rotation and its effective translation over the terrain. The longitudinal slip ratio is defined as follow:

$$s = \begin{cases} \frac{r\omega - v_x}{r\omega} & \text{if } r\omega \geq v_x \quad \text{(traction)} \\ \frac{r\omega - v_x}{v_x} & \text{if } v_x > r\omega \quad \text{(braking)} \end{cases} \tag{3.6}$$

Where:

- v_x is the longiotudinal velocity of the wheel ;
- ω is the angular velocity of the wheel.

Shear deformation

Considering a wheel subjected to a certain slip ratio and a slip angle α, the shear displacements are considered as the soil deformations under the wheel as a function of the angle θ along the contact arc:

$$\begin{cases} j_x(\theta) = r\left[(\theta_f - \theta) - (1-s)(\sin\theta_f - \sin\theta)\right] \\ j_y(\theta) = r(1-s)(\theta_f - \theta)\tan\alpha \end{cases} \tag{3.7}$$

Assuming the small-angle hypothesis ($\sin\theta \approx \theta$) and evaluating the displacement at the end of the contact arc (where the arc length is $l \approx r\theta_f$ and θ=θ_r=0), the linearized expressions are obtained:

$$\begin{cases} j_x \approx s \cdot l \\ j_y \approx (1-s) \cdot l \cdot \tan\alpha \end{cases} \tag{3.8}$$

The total shear displacement j_{tot}, which represents the magnitude of the deformation imparted to the terrain, is given by the vector resultant:

$$j_{tot} = \sqrt{j_x^2 + j_y^2} = l\sqrt{s^2 + \left[(1-s)\tan\alpha\right]^2} \tag{3.9}$$

Shear stress

From the Janosi-Hanamoto formulation of shear stresses, the following formulation is obtained:

$$\tau = \tau_{\max}\left(1 - e^{-\frac{j}{K}}\right) \tag{3.10}$$

Substituting the Mohr-Coulomb failure condition (Eq. 3.5), the complete formulation becomes:

$$\tau = \left[c + p\tan(\phi)\right]\left(1 - e^{-\frac{j}{K}}\right) \tag{3.11}$$

3.3 Longitudinal Forces Formulation

In this paragraph it is exposed a simple model for longitudinal wheel-force interaction proposed by NASA technical literature [13].

Gross Traction

The gross tractive force H is obtained by integrating the local shear stress $\tau(\theta)$ over the entire contact area. By assuming a uniform pressure distribution and linearizing the shear displacement along the contact length l, as proposed in the NASA technical model [13], the following analytical formulation is obtained:

$$H = (Ac + W\tan\phi)\left[1 - \frac{K}{sl}\left(1 - e^{-\frac{sl}{K}}\right)\right] \tag{3.12}$$

Noticing that $j_t = sl$, this equation can be rewritten:

$$H = (Ac + W\tan\phi)\left[1 - \frac{K}{j_x}\left(1 - e^{-\frac{j_x}{K}}\right)\right] \tag{3.13}$$

Compaction resistance

When the wheel passes over the soft lunar soil, the soil deforms and compacts. This compaction produces a resistance to the wheel's motion called compaction resistance. The formulation of the compaction resistance equation from [13] is as follows:

$$R_c = \frac{(k_c + k_\phi b)z^{n+1}}{n+1} \tag{3.14}$$

Substituting the sinkage equation 3.2, we obtain:

$$R_c = \frac{1}{n+1}\left(\frac{3}{3-n}\frac{W}{\sqrt{D}}\right)^{\frac{2(n+1)}{2n+1}}\frac{1}{k_c + bk_\phi}^{\frac{1}{2n+1}} \tag{3.15}$$

For Lunar soil with $n = 1.0$, the equation becomes:

$$R_c \approx 0.85854\left[\frac{W^4}{(k_c + bk_\phi)D^2}\right]^{1/3} \tag{3.16}$$

Bulldozing resistance

During motion, the wheel tends to accumulate a portion of soil in front of itself, generating a resistance called bulldozing resistance. The formulation of the bulldozing resistance proposed by [13] is the following:

$$R_b = \frac{b\sin(\theta_f + \phi)}{2\sin\theta_f \cos\phi}\left(2zcK_c + \gamma z^2 K_\gamma\right) + \frac{l_0^3\gamma}{3}\left(\frac{\pi}{2} - \phi\right) + cl_0^2\left[1 + \tan\left(\frac{\pi}{4} + \frac{\phi}{2}\right)\right] \tag{3.17}$$

$$l_0 = z\tan^2\left(\frac{\pi}{4} - \frac{\phi}{2}\right) \tag{3.18}$$

$$K_c = (N_c - \tan\phi)\cos^2\phi \tag{3.19}$$

$$K_\gamma = \left(\frac{2N_\gamma}{\tan\phi} + 1\right)\cos^2\phi \tag{3.20}$$

where:

- l_0 is the length of soil ruptured by compression;
- K_c: cohesive modulus of soil deformation;
- K_γ: density modulus of soil deformation.

Drawbar-Pull

In the longitudinal direction, the drawbar-pull is defined as the net force applied to the wheel and can be calculated as the tractive force minus the sum of the resistances:

$$DP = H - R_c - R_b \tag{3.21}$$

The resistance are always opposed to the wheel velicty v_x as can be seen in figure 3.4

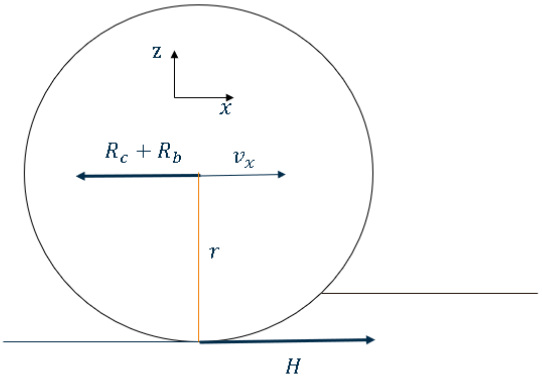

Figure 3.4: Free-body diagram of a driven rigid wheel where gross traction H is opposed by the sum of motion resistances $(R_c + R_b)$.

3.4 Extension of the model to lateral force components

Traction force

To take into account the effects of the lateral forces created during steering maneuver in the equation the longitudinal slip j_x is approximated to the total slip j_{tot} 3.9:

$$H = (Ac + W \tan\phi)\left[1 - \frac{K}{j_{tot}}\left(1 - e^{-\frac{j_{tot}}{K}}\right)\right] \tag{3.22}$$

Where H in this case is the total force due to longitudinal and lateral shear stresses Since the gross tractive force H is generated by the tangential deformation of the soil, its direction coincides with that of the total shear displacement j_{tot}. In a combined maneuver (longitudinal and lateral), the displacement vector is defined by its components j_x and j_y. To derive the forces acting on the wheel axes, it is assumed that the total force H is distributed proportionally to the contribution of each slip component. From here, the lateral and longitudinal force components on the wheels are obtained:

$$F_{x,gross} = H\frac{j_x}{j_{tot}}, \quad F_{y,gross} = H\frac{j_y}{j_{tot}} \tag{3.23}$$

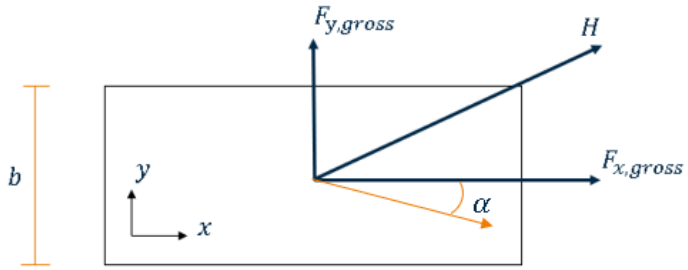

Figure 3.5: Top-view representation of the wheel with the decomposition of the total gross tractive force H into its longitudinal ($F_{x,gross}$) and lateral ($F_{y,gross}$) components.

Bulldozing resistance decomposition

In the model, it is assumed that the bulldozing resistance acts in both directions as a resistance to the local motion of the wheel. So the bulldozing resistance is decompoed along the side slip angle α. Longitudinally, bulldozing represents a resistance that opposes the longitudinal component of the tractive force. Laterally, however, bulldozing is a contribution to the lateral force because the soil acts as a physical barrier effectively increasing the lateral reaction force and preventing the rover from sliding sideways. The approximation made is to decompose the bulldozing resistance with respect to the wheel slip angle α so as to obtain the longitudinal and lateral components:

$$\begin{cases} R_{b,x} = R_b \cos|\alpha| \\ R_{b,y} = R_b \sin|\alpha| \end{cases} \tag{3.24}$$

Net force formulation

Having performed the decomposition of the total shear force and the bulldozing, the following formulation of the total forces is obtained:

$$\begin{cases} F_{x,net} = F_{x,gross} - (R_c + R_{b,x}) \\ F_{y,net} = F_{y,gross} + R_{b,y} \end{cases} \tag{3.25}$$

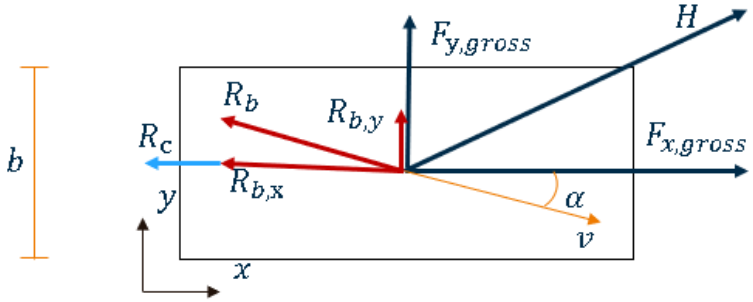

Figure 3.6: Vectorial representation of the wheel forces in the $x - y$ planes the interaction between gross tractive components ($F_{x,gross}, F_{y,gross}$) and motion resistances (R_c, R_b).

3.5 Torque

Considering the veichle in motion, the torque needed to keep the motion steady is computed as follow:

$$T_{min} = r(R_c + R_{b,x}) \tag{3.26}$$

In order to increase the speed, it is necessary that:

$$T_{app} > T_{min} \tag{3.27}$$

3.6 Lunar Soil Parameters

The lunar soil parameters are listed in Table 3.1

Symbol	Description	Lunar Soil Value
n	Exponent of sinkage	1.0
k_c	Cohesive modulus	$1400\,N/m^2$
k_ϕ	Frictional modulus	$820{,}000\,N/m^3$
ϕ	Angle of internal friction	$30-40$ degree
c	Cohesive strength of soil	$170\,N/m^2$
γ	Soil weight density	$2470\,N/m^3$
K	Coefficient of soil slip	$0.018\,m$
N_q	Terzaghi's bearing capacity factor	32.23
N_c	Cohesive bearing capacity factor	48.09
N_γ	Density bearing capacity factor	33.27
K_c	Cohesive modulus of soil deformation	33.37
K_γ	Density modulus of soil deformation	72.77

Table 3.1: Lunar Soil Parameters

[13]

3.7 Model Assumptions and limitations

In this section, the limitations of the terramechanical model presented are outlined. The following simplifying assumptions have been made:

- **Uniform Pressure Distribution:** The model utilizes the Bekker formulation based on a uniform pressure assumption. As noted in Section 3.1, real pressure distributions along the contact arc has a non linear trend . This simplification can lead to an overestimation of the vertical load-bearing capacity and inaccuracies in the calculated contact area A.
- **Neglect of Dynamic Sinkage:** The model considers only static sinkage. In reality, as the slip ratio s increases, the soil is "excavated" by the wheel (slip-sinkage), leading to a deeper penetration than predicted by Equation 3.2.
- **Linearized Shear Displacement:** The shear displacement j is linearized along the contact arc. This assumes the deformation grows linearly from entry to exit, which may not be true under extreme slip conditions or high sinkage.
- **Zero Elastic Recovery:** By assuming the exit angle $\theta_r = 0$, the model ignores the elastic rebound of the soil. This prevents the calculation of the small amount of forward thrust or resistance generated at the rear of the contact patch.

- **Bulldozing decomposition:** The decomposition of the bulldozing resistance R_b using the slip angle α (Eq. 3.24) represents a geometric approximation, as the original formulation specifically addresses longitudinal bulldozing. In this work, a simplifying hypothesis is adopted, assuming that the bulldozing resistance is isotropic with respect to the local motion direction. Consequently, R_b is geometrically projected onto the components of the wheel reference frame using the side-slip angle α.
- **Small Angle Hypothesis:** The linearization of j_x and j_y relies on the assumption $\sin\theta \approx \theta$. For large entry angles θ_f (associated with high sinkage z), this approximation loses accuracy, potentially distorting the force components calculation.
- **Rigid Wheel:** The model neglects the effect of the wheel deformations.

Chapter 4

Simulink Implementation

This chapter describes the functioning of the model. The software Simulink was used for the model's development. The vehicle dynamics equations reported in Chapter 2 and the simplified terramechanics model equations reported in Chapter 3 are integrated within the model. The development of the model required several phases:

- Development of the suspension model, which required the implementation of the vertical dynamics equations described in Chapter 2;
- Development of the vehicle dynamic model, which required the implementation of the plane dynamics equations described in Chapter 2;
- Development of a terramechanics model for the simulation of wheel-soil contact forces using the set of equations reported in Chapter 3.

4.0.1 Model setup

In order to run a simulation, the model requires inputs and parameters regarding the vehicle, the initial conditions, and the soil coefficients.

Input

There are two model inputs:

- The torque provided to the wheels;
- The steering angle δ_i.

Depending on the chosen rover configuration, torque and steering angle can be provided to more or fewer wheels. Indeed, the inputs enter the wheel block and

are managed individually by each of these blocks. This allows for parameterization based on the vehicle configuration, particularly regarding the steering system and the traction type:

- The vehicle can be managed as Front-Wheel Drive (FWD), Rear-Wheel Drive (RWD), or All-Wheel Drive (AWD);
- The vehicle can be configured with a classic Ackermann steering system, by providing the steering input only to the front wheels, or a dual Ackermann system by also steering the rear wheels.

By keeping the steering at 0 on each wheel and varying the torque between the right and left sides of the rover, it is possible to make the steering system "skid steering". However, this option was not taken into consideration in the analyses performed because it would require complex feedback control of the torque.

Number of wheels and position

One of the fundamental parameters taken into account during the model development was the management of the number of wheels. In fact, the model receives the number of wheels as a parameter, which, depending on the configuration, can be 4, 6 (with the addition of two central wheels), or 8 (with the addition of 4 central wheels). In the Simulink model, this is managed via the "enable subsystem" block, which activates the central wheel blocks according to the defined number of wheels.

To ensure a robust management of the modular configuration, a specific numbering convention has been established. This indexing is crucial for the correct assignment of the geometric parameters and the distribution of the control signals (torque and steering) from the main controller to the individual wheel subsystems.The wheels are numbered following a "Z" pattern, starting from the front-left and moving to the rear-right. The convention adopted for the maximum configuration (8 wheels) is as follows:

- **Wheels 1 and 2:** Front axle (Left and Right);
- **Wheels 3 and 4:** First central axle (Left and Right);
- **Wheels 5 and 6:** Second central axle (Left and Right);
- **Wheels 7 and 8:** Rear axle (Left and Right).

In the case of a 4-wheel or 6-wheel configuration, the "Enabled Subsystem" blocks automatically deactivate the intermediate indices. For example, in a standard 4-wheel setup, only wheels 1-2 (front) and 7-8 (rear) are active, ensuring that the longitudinal distances x_f and x_r correctly reflect the wheelbase of the rover. This

numbering system also facilitates the calculation of the pitch and roll moments within the Chassis Dynamics block, as each force $F_{z,i}$ is multiplied by its specific coordinate according to its index i. The frontal and rear arms, L_f and L_r, and the two lateral arms, L_r and L_f (typically equal and set to half of the wheel track), are provided as inputs. From these, a dedicated code—depending on the number of wheels chosen for the configuration—assigns the arms to the wheel block in such a way as to keep the wheels equidistant.

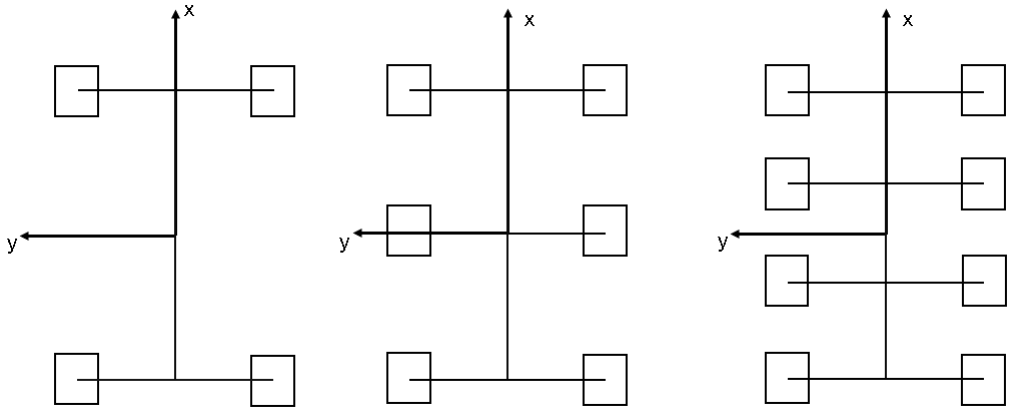

Figure 4.1: Planar layout of the 4, 6, and 8-wheel rover configurations. The reference frame is centered at the center of gravity (CoG), with the x-axis representing the longitudinal direction and the y-axis the lateral direction.

Masses and Geometries

The following mass and geometric parameters are assigned to the vehicle:

- **Mass and Inertia properties:**
  - M_s: Sprung mass of the vehicle;
  - I_{xx}, I_{yy}, I_{zz}: Moments of inertia for roll, pitch, and yaw axes;
- **Geometric parameters:**
  - L_f, L_r: Frontal and rear longitudinal arms;
  - b_f, b_r: Lateral arms (half-track width);
  - h_r: Distance from the Center of Gravity (CG) to the pitch and roll axes;

Wheels and Suspensions Parameters

Each suspension and wheel assembly is assigned the following parameters:

- **Wheel parameters:**
  - d: Wheel width;
  - r: Wheel radius;
  - I_w: Wheel rotational inertia;
  - k_u: Radial stiffness of the tire/wheel.
- **Suspension parameters:**
  - k_s: Elastic stiffness coefficient of the suspension spring;
  - m_u: Unsprung mass;
  - c_s: Damping coefficient of the suspension shock absorber.

4.0.2 Model workflow

The simulation follows a closed-loop architecture where the state of the vehicle is continuously updated based on the interaction between the subsystems. The high-level signal flow is illustrated in Figure 4.2. The workflow can be summarized as follows:

- **Model Inputs:** The simulation is initialized with the control inputs (torque and steering) and the physical parameters of the rover.
- **Wheels and Suspensions:** This block receives the inputs and the current state of the chassis (displacements and velocities). It calculates the contact forces F and moments M generated by the interaction with the soil and the suspension travel.
- **Chassis Dynamics:** Acting as the core of the model, this 6-DoF block solves the equations of motion for heave, pitch, and roll. It processes the forces and moments to compute the local accelerations and velocities ($V_{x,local}, V_{y,local}$).
- **Trajectory and State Output:** The local velocities are integrated and transformed into global coordinates (x_{global}, y_{global}) to plot the planar trajectory. Simultaneously, the CG pose (roll ϕ, pitch θ, yaw ψ, and heave z) is exported as the primary state output.

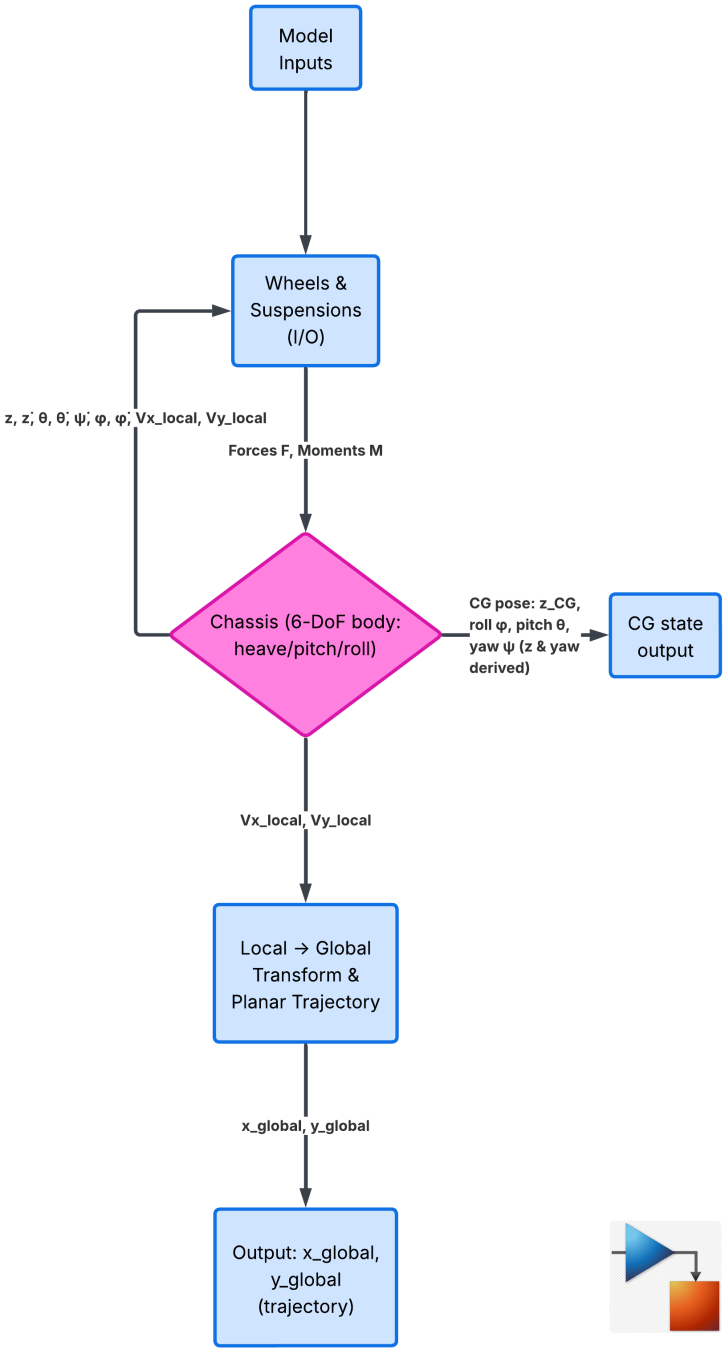

Figure 4.2: Functional block diagram of the Simulink model. The diagram shows the feedback loop between the Wheels/Suspensions block and the Chassis Dynamics core, including the local-to-global transformation for trajectory tracking.

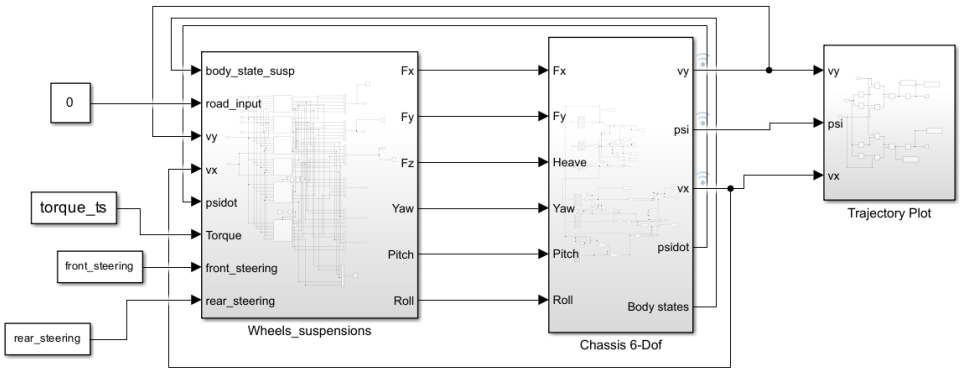

Figure 4.3: Full simulink model.

4.1 Wheel-Suspension System

The Wheel-Suspension (WS) system contains the individual blocks for each suspension unit, which are composed of a wheel block and a suspension block. These two components communicate primarily through the vertical contact force F_z, calculated within the suspension block using Equation 2.43. Once the forces are computed, the resulting moments are determined by multiplying the forces by their respective lever arms x_i and y_i.

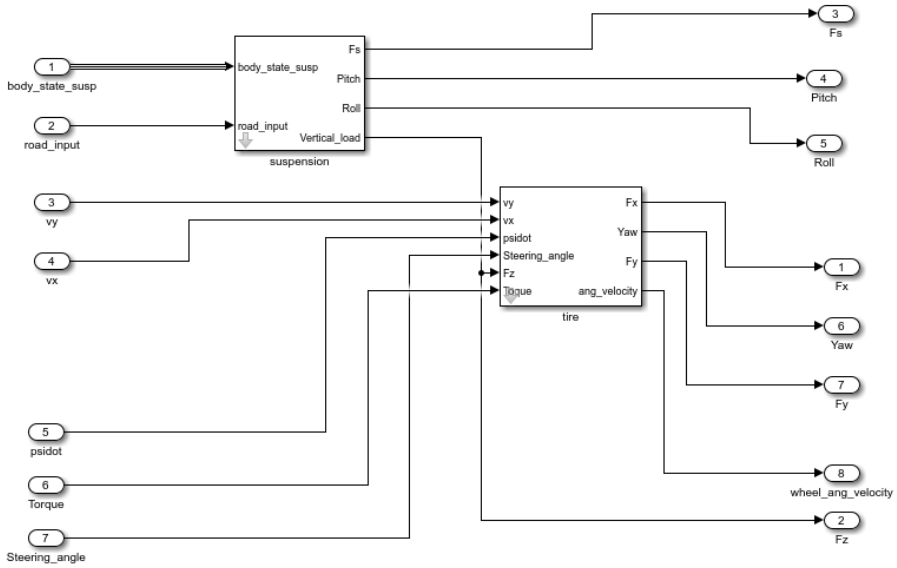

Figure 4.4: Simulink implementation of the single Wheel-Suspension assembly, showing the interconnection between the suspension dynamics and the tire model.

4.1.1 Suspension block

This block implements the equations of vertical dynamics to calculate the vertical suspension force F_z and the resulting pitch and roll moments. It also outputs the vertical load acting on the wheel, which is then fed as an input to the wheel block. The block receives the following inputs:

- z: Vertical displacement of the Center of Gravity (CG) and its velocity $\dot{z}$;
- θ: Pitch angle and its angular velocity $\dot{\theta}$;
- ϕ: Roll angle and its angular velocity $\dot{\phi}$;
- z_r: Vertical displacement of the terrain, set to 0 for the full-model simulations in order to simulate a planar terrain.

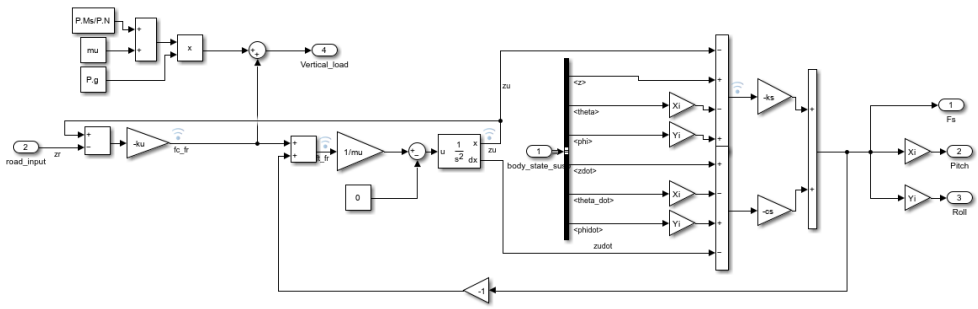

Figure 4.5: Simulink implementattion of the suspension block

4.1.2 Wheel block

This block calculates the longitudinal (F_x) and lateral (F_y) wheel-soil interaction forces and teh relatives resistance forces, as well as the wheel's contribution to the total yaw moment. The wheel block receives the following inputs:

- $\dot{\psi}$: Yaw angular velocity;
- v_x, v_y: Velocities in the local reference frame;
- δ_i: Steering angle for the specific wheel;
- T: Applied torque.
- F_z: Vertical load on the wheel.

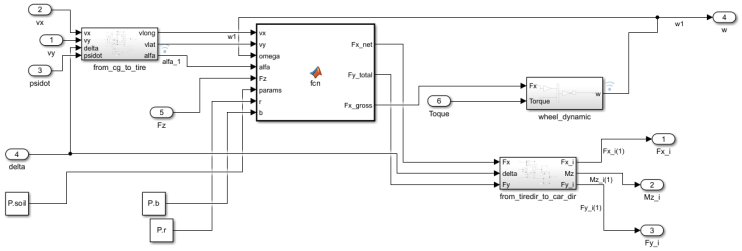

Figure 4.6: Simulink implementation of the wheel block

The internal architecture of the Wheel Block follows a closed-loop dynamic structure. Initially, the Velocity Rotation Block translates the global chassis motion into local

wheel kinematics, calculating the longitudinal velocity v_{xt}, lateral velocity v_{yt}, and the side-slip angle α using Equations 2.29, 2.31, and 2.30. These velocities are then rotated with respect to the steering angle δ to obtain v_x^w and v_y^w in the wheel reference frame. The velocities in the wheel reference frame, wheel's angular velocity ω and wheel's vertical load F_z are processed by the Wheel-Soil Interaction Block (WSIB) to determine forces and resistances based on lunar regolith parameters. A feedback loop is established with the Wheel Dynamics Block, where the balance between the applied torque and the longitudinal tractive force determines the wheel's rotational acceleration $\dot{\omega}$, that is integrated to obtain angular velocity ω. Finally, the Forces Rotation Block rotates the total force resultants from the wheel reference frame back to the vehicle's Center of Gravity (CG) reference frame to contribute to the overall longitudinal, lateral, and yaw dynamics using the rotation matrix Equation 2.39.

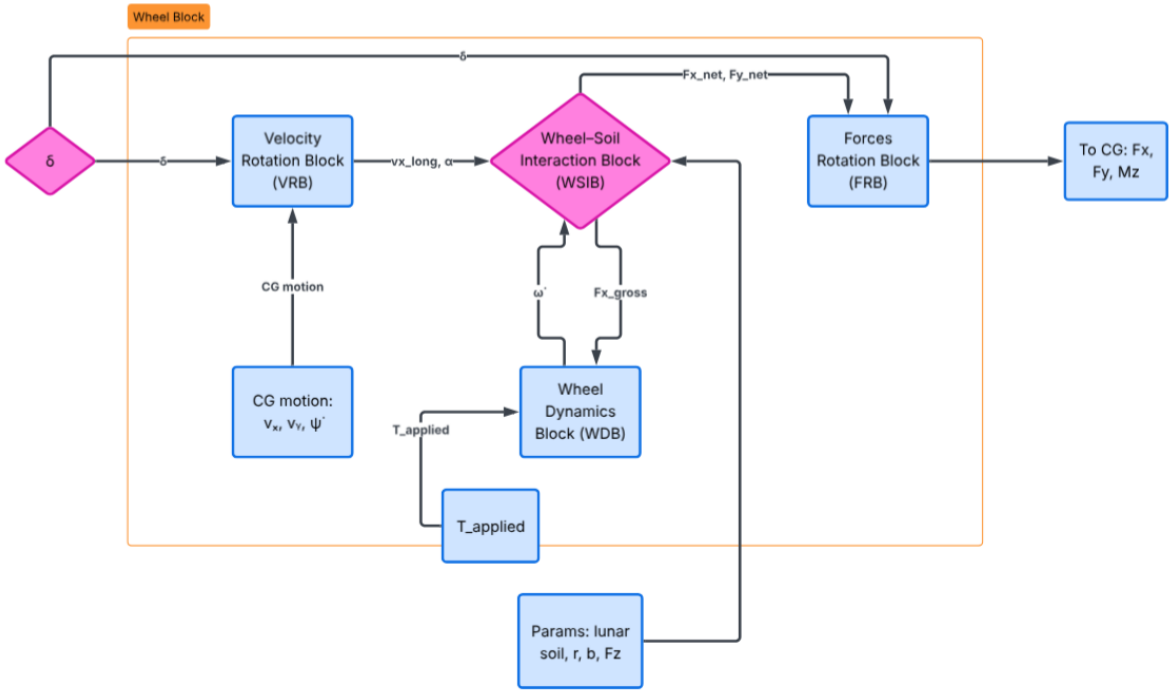

Figure 4.7: Functional block diagram of the Wheel Unit.

Velocity rotation block

This component utilizes Equation 2.29 to calculate the slip angle α, as well as the longitudinal and lateral velocities within the wheel's local reference frame.

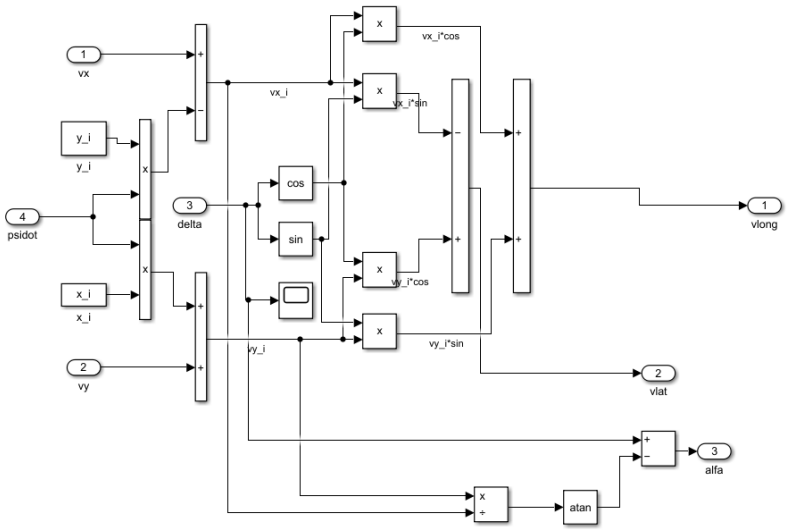

Figure 4.8: Simulink implementation of the Velocity Rotation Block.

Wheel-soil interaction block

This block receives the longitudinal velocity, the slip angle, the wheel's angular velocity, and the vertical contact force to calculate the forces F_x and F_y and the relative resistance forces using the equations detailed in Chapter 3. This block is implemented using a "MATLAB Function block".

Wheel Dynamics block

This block receives the input torque and the tractive force calculated in the Wheel-Soil Interaction Block to compute the wheel's angular velocity, which is then fed back into the interaction block. This block utilizes equation 2.44 in order to integrate wheel rotational velocity having as an input the applied torue and the traction force produced by shear displacment in the longitudinal direction.

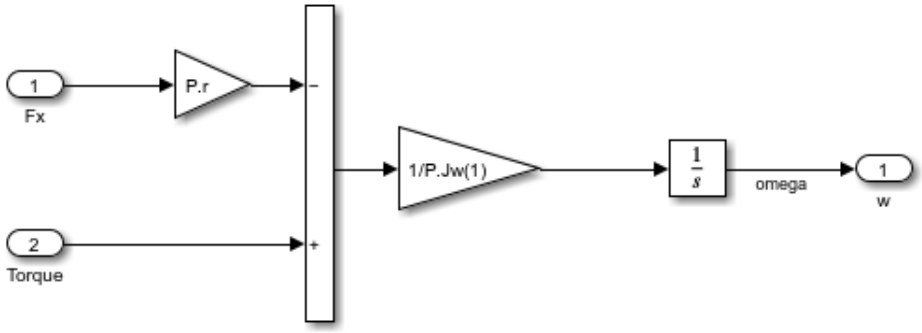

Figure 4.9: Simulink implementation of wheel dynamics. This block utilizes dynamics equation of the wheel to compute wheel angular velocity.

Forces rotation block

This block rotates the forces from the wheel's reference frame back to the local vehicle reference frame and sends these forces to the Chassis Dynamics block.

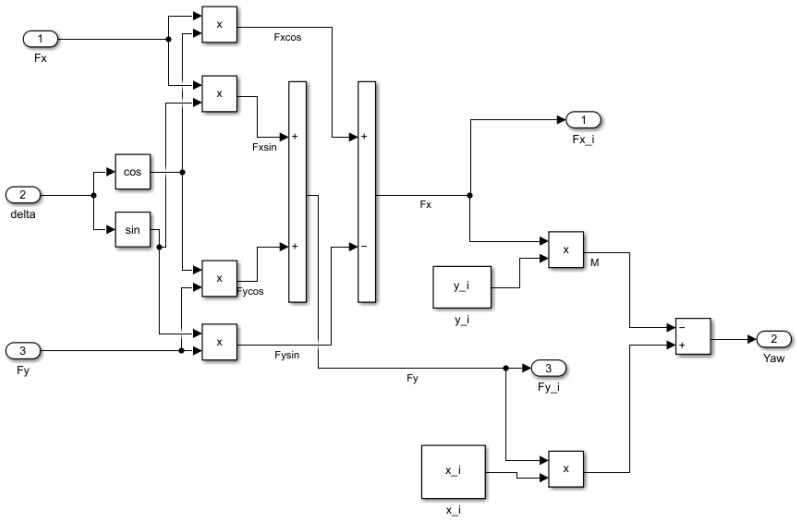

Figure 4.10: Simulink implementattion for the Forces Rotation Block. It maps wheel-frame forces back to the chassis frame and calculates the yaw moment contribution for each wheel unit.

4.2 Chassis Dynamics

This block contains the equations related to the vehicle dynamics. It receives the forces and moments calculated in the wheel-suspension system block as inputs. As outputs, it returns the translational and angular velocities of the center of mass. These outputs are subsequently saved and plotted using a dedicated MATLAB script.

Heave

By receiving the vertical suspension forces as inputs, the block calculates the vertical acceleration of the center of mass using Equation 2.22. Through a double integrator, the vertical velocity and displacement of the center of mass are then respectively calculated.

Pitch

By receiving the contributions of the vertical suspension forces to the pitch moment, the block calculates the angular acceleration of the pitch angle $\ddot{\theta}$ using Equation 2.42. From this, through a double integrator, it calculates the pitch rate $\dot{\theta}$ and the pitch angle θ.

Roll

By receiving the contributions of the vertical suspension forces to the roll moment, the block calculates the angular acceleration of the roll angle $\ddot{\phi}$ using Equation 2.41. From this, through a double integrator, it calculates the roll rate $\dot{\phi}$ and the roll angle ϕ.

Yaw

By receiving the contributions of the wheel contact forces F_x and F_y to the yaw moment, the block calculates the angular acceleration of the yaw angle $\ddot{\psi}$ using Equation 2.40. From this, through a double integrator, it calculates the yaw rate $\dot{\psi}$ and the yaw angle ψ.

Planar velocity

Using the forces F_x and F_y of the individual wheels, already rotated into the local reference frame, the block utilizes Equations 2.36 and 2.38 to calculate the longitudinal and lateral accelerations in the local reference frame of the center of mass. Through a single integration, the longitudinal and lateral velocities of the center of mass are then determined.

4.3 Trajectory Plot

This block receives the planar velocities v_x and v_y of the center of mass in the local reference frame, along with the yaw angle ψ, and transforms the velocities from the local to the global reference frame using Equation 2.27. Through a single integration, the block then calculates the X and Y displacements in the global reference frame. These coordinates are saved, and the trajectory of the rover's center of mass is plotted using a specific MATLAB function.

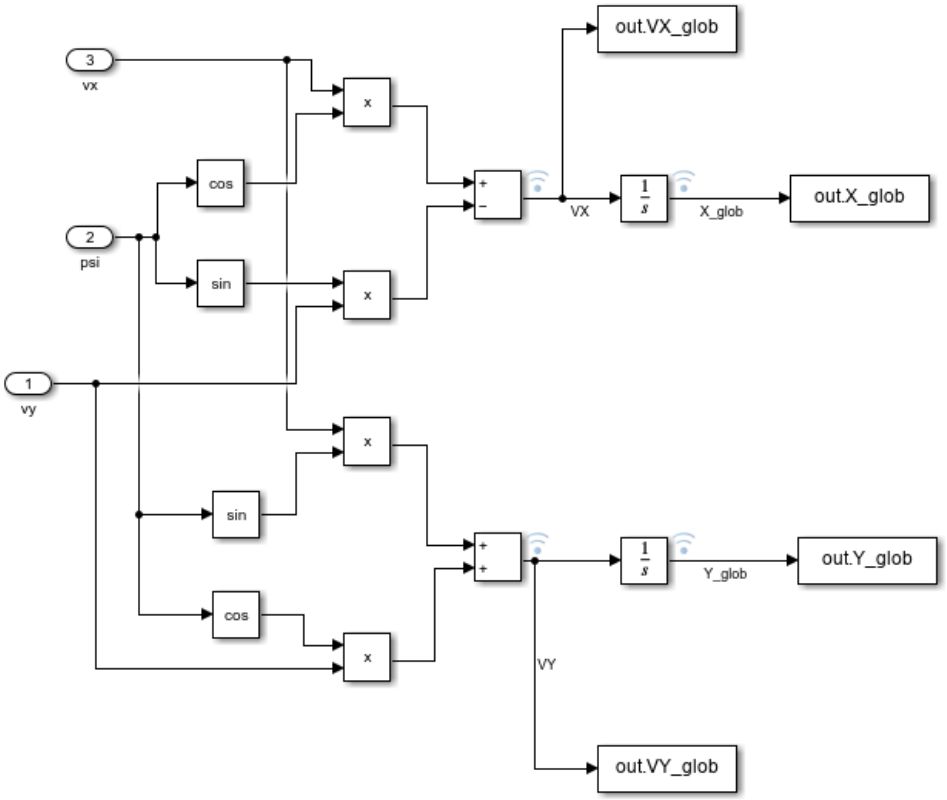

Figure 4.11: Simulink implementation of the coordinate transformation block. The logic converts local velocities (v_x, v_y) into global velocities (VX, VY)

Chapter 5

Analysis and Results

5.1 Baseline Configuration and Analysis Parameters

In this section, the parameters used for the analyses are presented. The masses and geometries of the main structure remain the same for every configuration.Other parameters, such as the suspension system coefficients, vary based on the number of wheels of the configuration under examination.

Main structure mass, geometry and inertia

The rover has a cylindrical shape. The mass of the structure and subsystems is approximated to the sprung mass m_s. The center of gravity is placed at the geometric center. The parameters just described are reported in Table 5.1:

Parameter	Symbol	Value	Unit
Sprung Mass	m_s	4000	kg
Unsprung Masses	m_u	100	kg
Total Length	L	5.2	m
Radius	R	1.8	m
Track Width (Diameter)	W	3.6	m
Lateral Distance (Left/Right)	$y_{l,r}$	1.8	m
Moment Arms (CG to Roll and Pitch Axis)	$h_r = h_P$	0.9	m
Distance CG to Front Axle	x_f	2.6	m
Distance CG to Rear Axle	x_r	2.6	m

Table 5.1: Mass and geometry parameters.

The unsprung mass m_u is set constant across all configurations. This value was selected to maintain the unsprung-to-sprung mass ratio $\mu = \frac{m_u}{m_{sw}}$ within the range typical for off-road vehicles (0.10–0.20), where m_{sw} represents the portion of the sprung mass supported by each wheel under static conditions:

$$m_{sw} = \frac{m_s}{N} \tag{5.1}$$

The following equations define the moments of inertia used in the rover's dynamic model:

- **Roll Moment of Inertia (I_{xx})** Calculated based on the mass distribution across the track width:
$$I_{xx} = \frac{1}{2} \cdot m_s \cdot R^2 \tag{5.2}$$
- **Pitch Moment of Inertia (I_{yy})** Calculated based on the longitudinal distance between axles:
$$I_{yy} = \frac{1}{12} m_s \cdot L^2 + \frac{1}{4} m_s R^2 \tag{5.3}$$

Wheel geometries and inertia

The wheel dimensions are reported in Table 5.2:

Parameter	Symbol	Value	Unit
Wheel Radius	r	0.5	m
Wheel Width	b	0.4	m

Table 5.2: Wheel dimensions.

The wheel rotational inertia is estimated assuming that the wheel mass, approximately 30% of the unsprung mass, is distributed along the outer rim, yielding:

$$I_w = 0.3 \cdot m_u \cdot r^2 \tag{5.4}$$

Suspension coefficients

For the calculation of the suspension stiffness and damping coefficients, the vehicle is approximated as a quarter-car model, presented in Chapter 2. Using Equations 2.4 and 2.5, and applying the Fourier transform, the values of k_s and c_s can be expressed as a function of the natural frequency of the sprung mass and the damping ratio ζ:

$$k_s = (2\pi f_n)^2 \cdot m_{sw}, \qquad c_s = 2\zeta\sqrt{k_s \cdot m_{sw}} \tag{5.5}$$

[14] In order to ensure astronaut comfort by limiting the vibration level of the sprung mass while maintaining adequate vibration isolation, the natural frequency f_n and damping ratio ζ are selected within typical ride-comfort design ranges. In particular, a low natural frequency is chosen to reduce transmitted accelerations, while a moderate damping ratio is adopted to avoid excessive oscillations without compromising isolation performance.

N	M_s [kg]	m_{sw} [kg]	f_n [Hz]	ζ [-]	k_s [N/m]	c_s [Ns/m]
4	4000	1000.0	1.2	0.5	56849	7540
6	4000	666.7	1.2	0.5	37899	5027
8	4000	500.0	1.2	0.5	28424	3770

Table 5.3: Suspension dynamic parameters calculated for each configuration.

Minimum torque calculation

To maintain a constant longitudinal velocity, the required driving torque is calculated using Equation 3.26. Figure 5.1 illustrates the trend of the longitudinal tractive force as a function of the slip ratio, alongside the respective motion resistances.

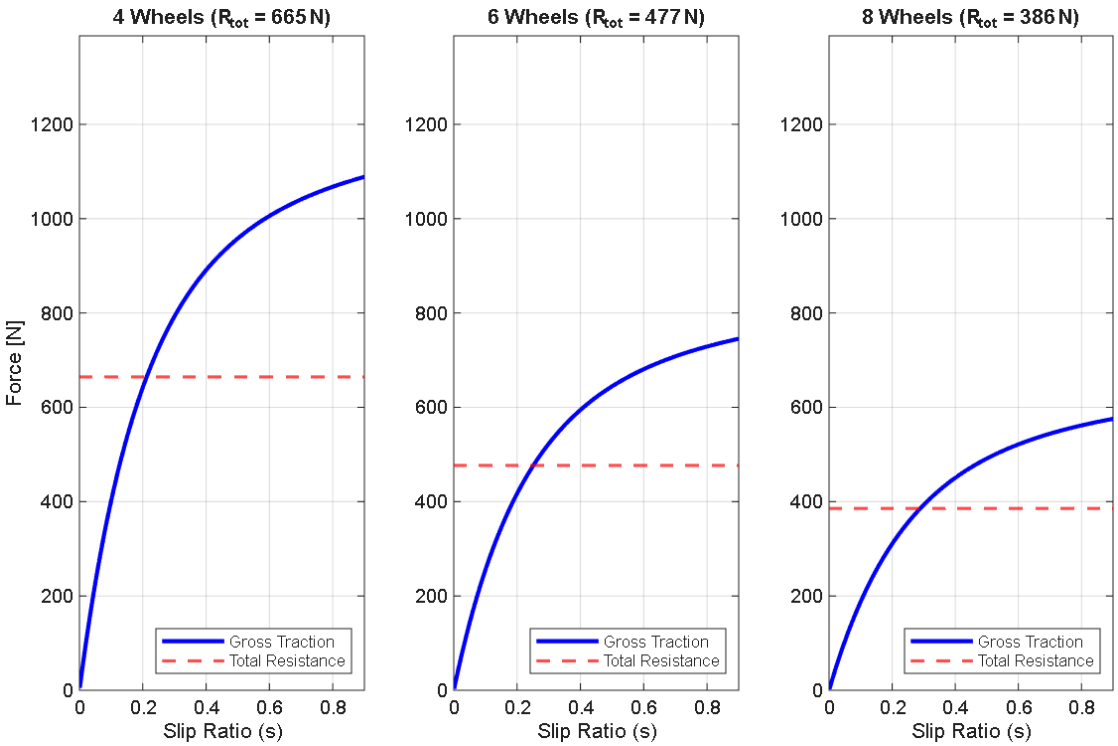

Figure 5.1: Preliminary traction performance analysis: comparison of Gross Traction and Total Resistance ($R_c + R_b$) for 4W, 6W, and 8W configurations at 4000 kg total mass.

The comparison shows that the maximum traction increases as the number of wheels decreases. This is due to the fact that, according to the Janosi-Hanamoto formulation, the maximum shear force depends directly on the vertical load acting on the wheel. The weight distribution per wheel varies significantly based on the configuration: a higher number of wheels results in a lower vertical load per unit, thereby reducing the maximum tractive force that a single wheel can generate. However, motion resistances also decrease as the number of wheels increases. These forces are directly dependent on the sinkage z, which is a function of the wheel load. Consequently, the equilibrium torque required to overcome these resistances is lower for the 8-wheel configuration and reaches its maximum for the 4-wheel case. Table 5.4 summarizes the sinkage and minimum torque values calculated for each configuration in static conditions.

Configuration	**Driving Torque** T [Nm]	**Static Sinkage** z [mm]
4 Wheels	332.3	40.4
6 Wheels	238.4	31.7
8 Wheels	192.8	27.0

Table 5.4: Steady-state performance comparison: Torque and Sinkage per wheel.

The 4W configuration is included for theoretical completeness. In a realistic scenario, a vehicle of this mass and wheelbase would likely deflect under its own self-weight without central supports. For this reason, while the 4W case is included in this preliminary analysis for comparison, its dynamic simulation results will be excluded from the following sections.

5.2 Acceleration and Coasting Maneuver - Comparison between 6-wheel and 8-wheel configurations

An initial velocity of 1 km/h is considered for this test. Each wheel is subjected to a constant driving torque equal to $T = 1.3T_{min}$ for a duration of 25 s. Subsequently, the torque is cut off, allowing the rover to proceed for 5 s without any tractive force. This setup simulates an initial acceleration phase followed by a coasting phase, where the vehicle advances by inertia while being progressively decelerated by motion resistances.

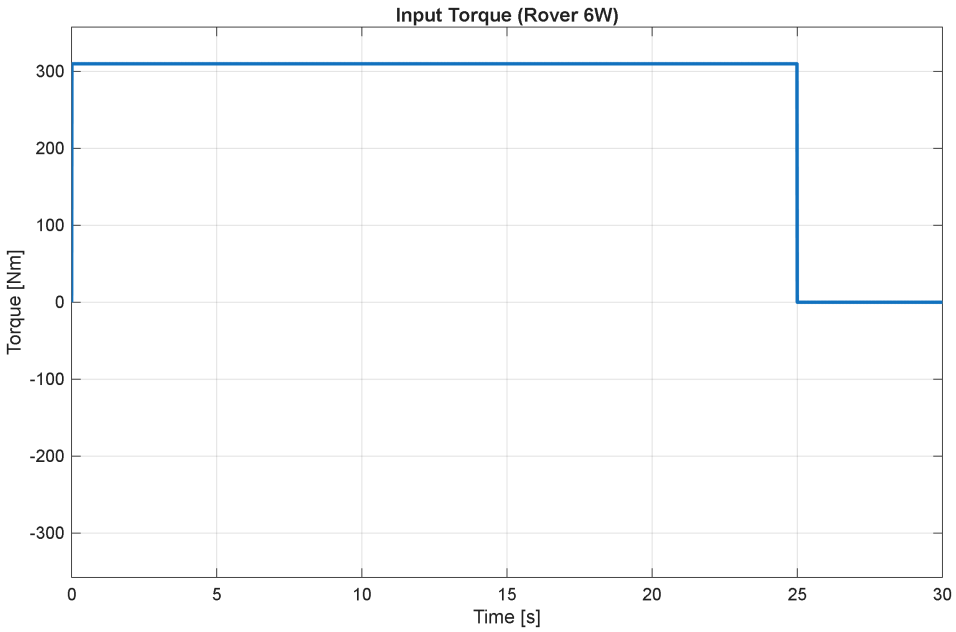

Figure 5.2: Input Torque profile for the 6-wheeled configuration.

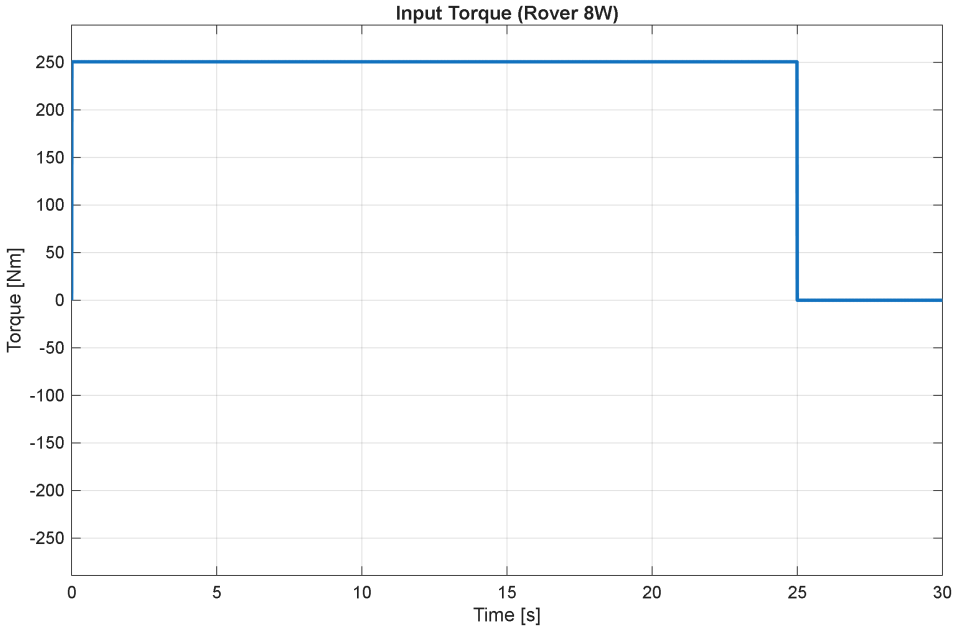

Figure 5.3: Input Torque profile for the 8-wheeled configuration.

5.2.1 Longitudinal Dynamics

Longitudinal Acceleration and Velocity

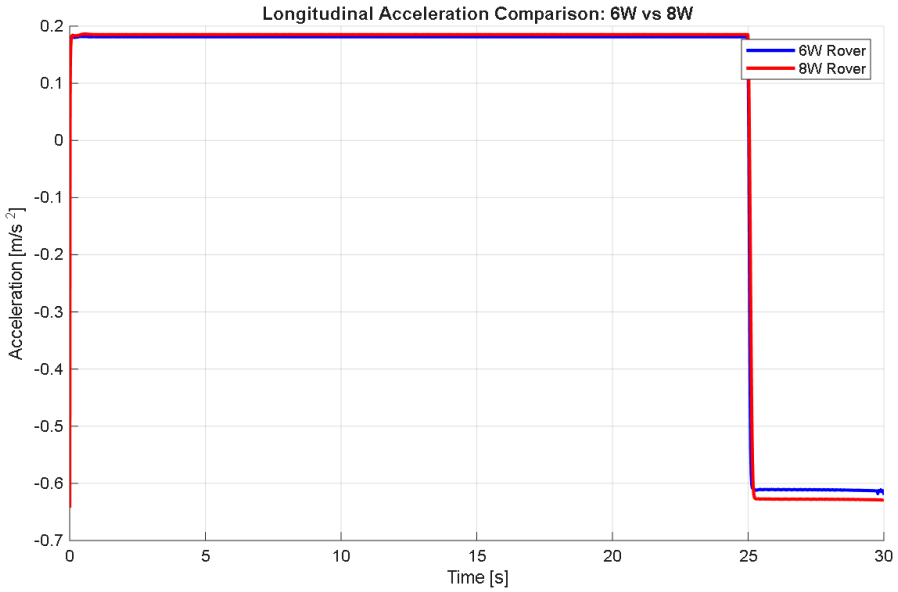

Figure 5.4: Comparison of longitudinal acceleration a_x.

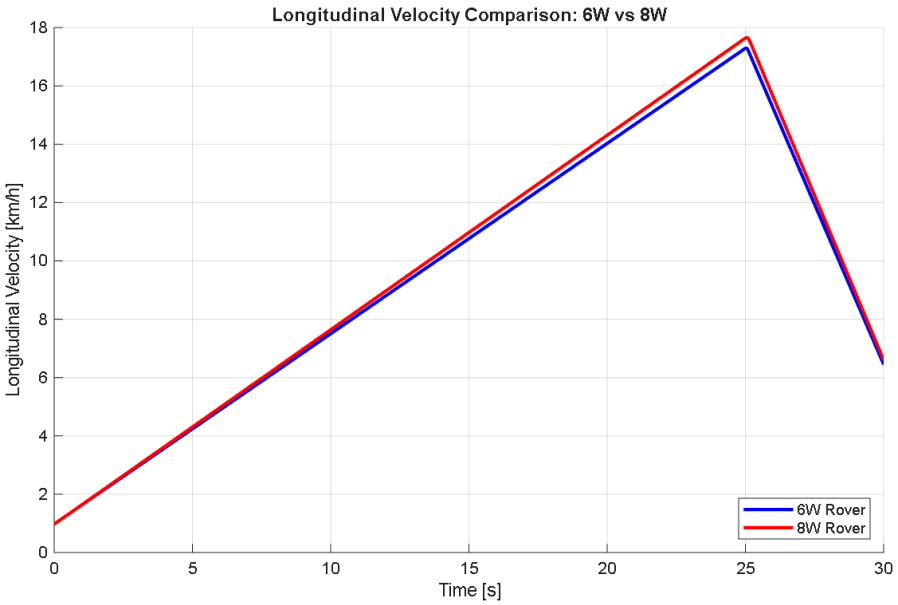

Figure 5.5: Comparison of longitudinal velocity v_x.

Figures 5.4 and 5.5 illustrate the acceleration phase during the first 25 s when the torque is applied. After the torque is cut off, the vehicle decelerates due to motion resistances. It can be observed that both acceleration and deceleration, in absolute terms, are slightly higher in the 8-wheeled configuration compared to the 6-wheeled one. The higher acceleration during the first phase is due to the fact that, although the tractive force per single wheel (at the same slip ratio) is lower in the 8W configuration, the additional wheels contribute to a slightly higher total longitudinal force (net of resistances) compared to the 6W configuration. The same principle applies to the coasting phase: while the individual resistance per wheel is higher in the 6W configuration, the cumulative total resistance acting on the 8W configuration is marginally greater.

5.2.2 Vehicle Attitude Response

Pitch

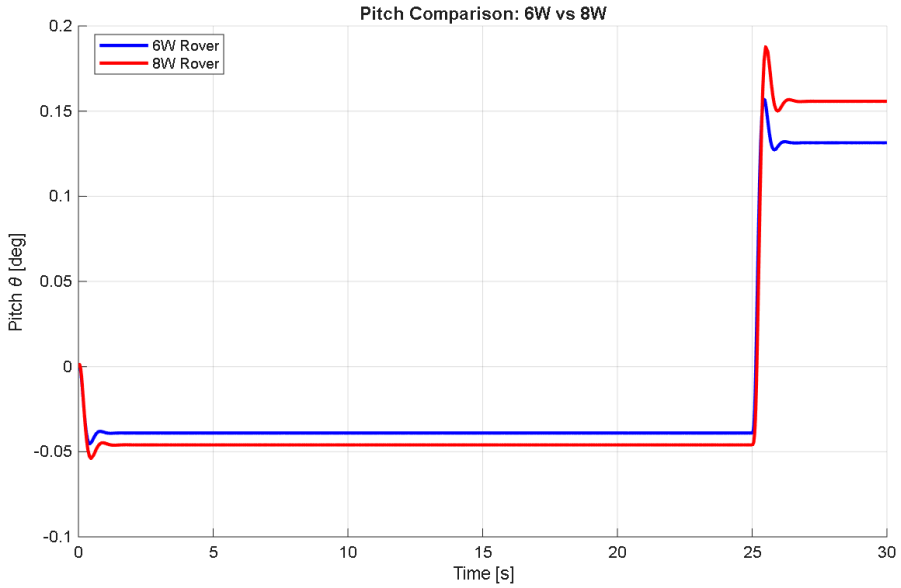

Figure 5.6: Comparison of pitch response.

During the acceleration phase, the front part of the vehicle rises, resulting in a negative pitch angle according to the chosen reference frame. When the vehicle starts to decelerate, the opposite occurs. Since the deceleration magnitude is greater than the acceleration magnitude, the pitch angle reaches a higher absolute value during the coasting phase.

Roll

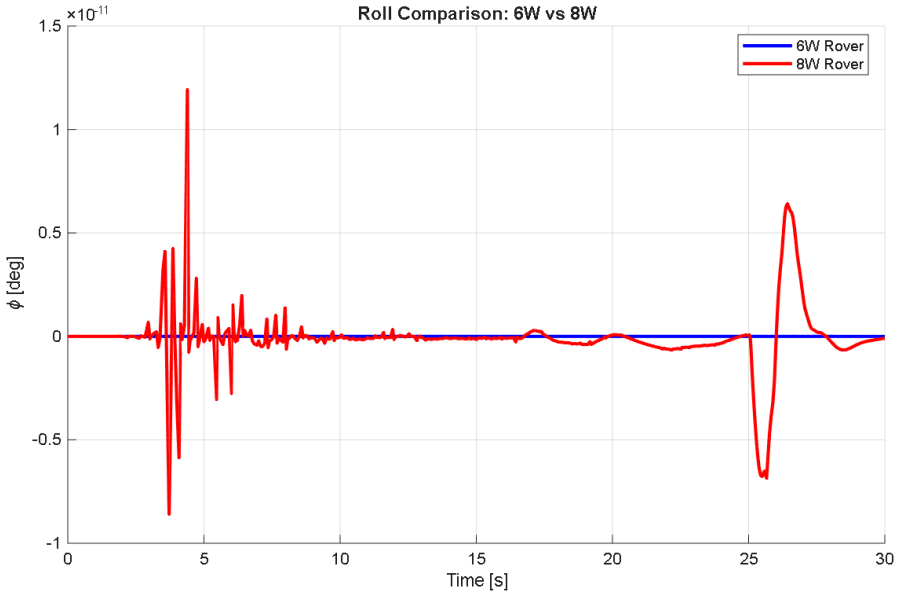

Figure 5.7: Comparison of roll response.

The roll angle remains null throughout the maneuver.

5.2.3 Wheel-Soil Interaction

Vertical Loads

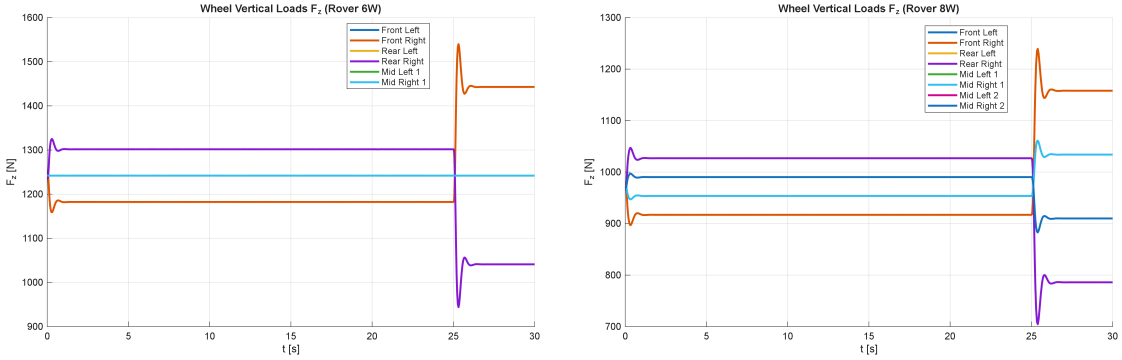

(a) 6-wheeled configuration **(b)** 8-wheeled configuration

Figure 5.8: Comparison of vertical wheel loads.

Due to the longitudinal load transfer, the rear wheels experience an increase in vertical load during acceleration, while the load on the front wheels decreases. In the 6-wheeled configuration, the central wheels (*Mid Left 1* and *Mid Right 1*) do not show variations in vertical load. This is because their longitudinal distance from the center of gravity is zero; therefore, inertial accelerations do not influence their vertical loading. In contrast, the four central wheels of the 8W configuration undergo a smaller load variation. During the coasting phase, the situation reverses: the front wheels become the most loaded, while the rear wheels experience the greatest load reduction.

Sinkages

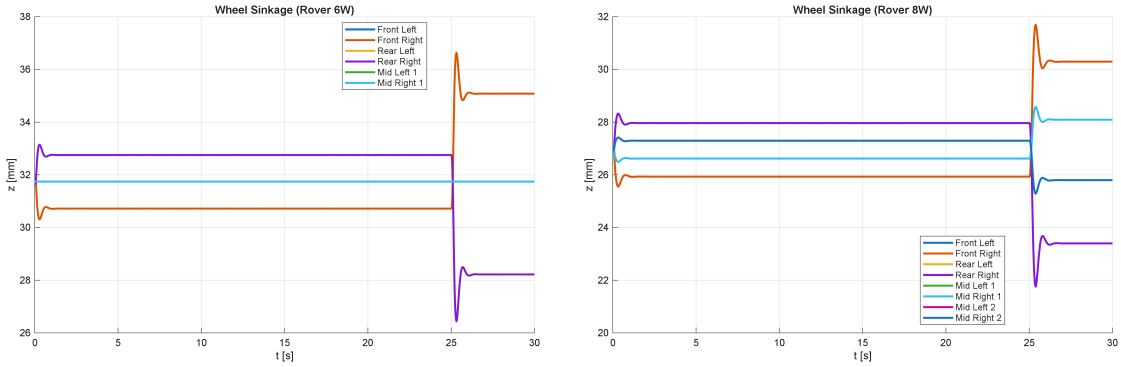

(a) 6-wheeled configuration **(b)** 8-wheeled configuration

Figure 5.9: Comparison of wheel sinkages.

The sinkage profiles follow the same trend as the vertical forces.

Longitudinal Forces

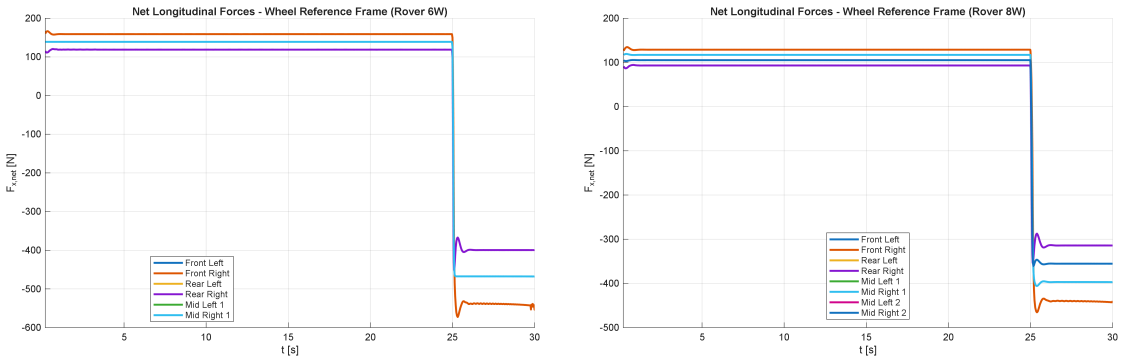

(a) 6-wheeled configuration **(b)** 8-wheeled configuration

Figure 5.10: Comparison of longitudinal wheel forces.

As discussed in the longitudinal dynamics section, the net longitudinal force per single wheel is higher in the 6W configuration. However, the total sum of the forces across all wheels is higher in the 8W configuration, resulting in a greater overall thrust. During the coasting phase, the forces become negative, indicating that traction is quasi null and only motion resistances are the main acting forces on the wheels.

Wheel Slip Ratios

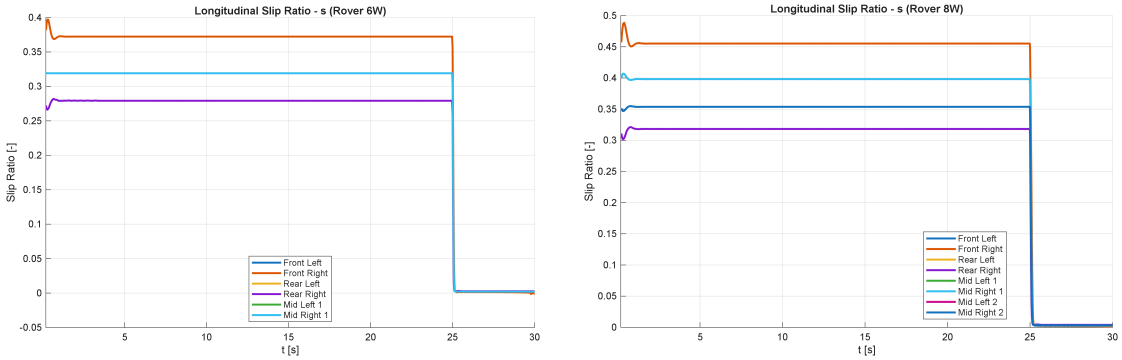

(a) 6-wheeled configuration **(b)** 8-wheeled configuration

Figure 5.11: Comparison of wheel slip ratios.

The longitudinal slip ratio drops close to zero when the torque is cut off, close to a pure rolling condition where no tractive forces are developed at the wheel-soil

interface.

Gross longitudinal Traction

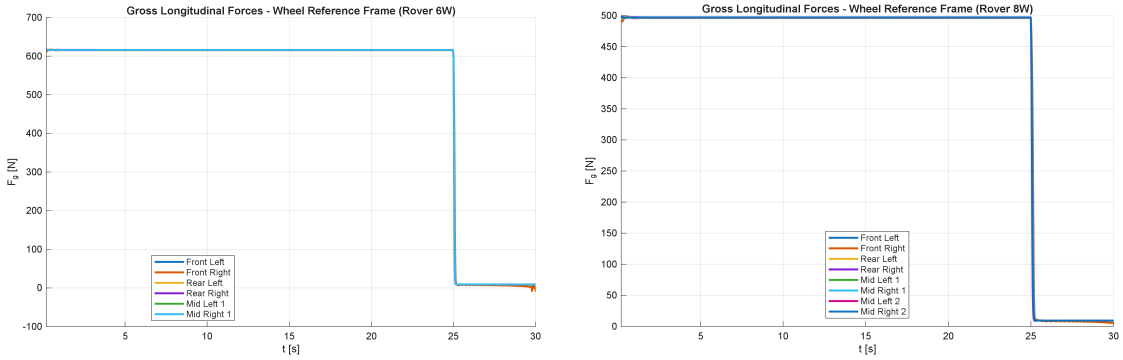

(a) 6-wheeled configuration **(b)** 8-wheeled configuration

Figure 5.12: Comparison of gross traction.

Wheel angular velocities

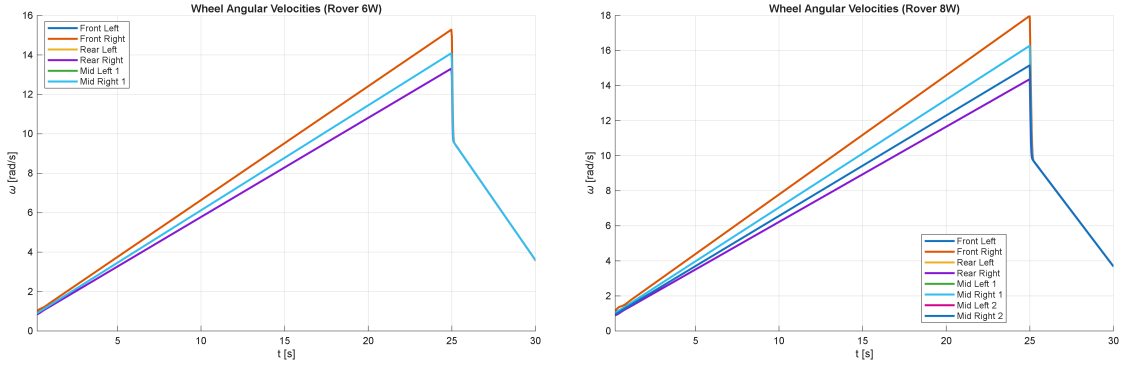

(a) 6-wheeled configuration **(b)** 8-wheeled configuration

Figure 5.13: Comparison of wheel angular velocity.

5.3 Front Steering

In this test, the vehicle is subjected to a *step steering input* applied exclusively to the front wheels in order to analyze the lateral dynamics of the system. The driving torque is set to the minimum value required to maintain a constant velocity. Starting from a velocity of 10 km/h, a steering angle of $\delta = 5°$ is applied at time $t = 1$ s for a duration of 9 s. Subsequently, the steering angle is returned to 0° for 10 seconds and, at time $t = 20$ s, a steering angle of $\delta = -5°$ is applied until the end of the test. This sequence simulates a left turn followed by a right turn at constant velocity.

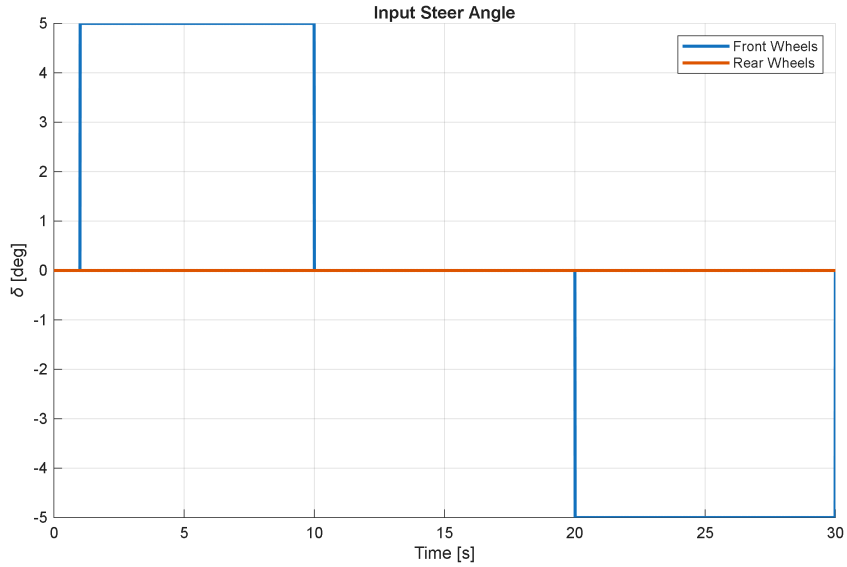

Figure 5.14: Steering Input profile (δ) over time.

It is noted that this configuration employs a *parallel steering geometry*. Although real-world vehicles typically implement Ackermann steering geometry — where the inner and outer wheel angles differ to prevent lateral scrubbing — the assumption of equal angles was considered an acceptable approximation for this study. This choice is justified by the rover's low operational speed.

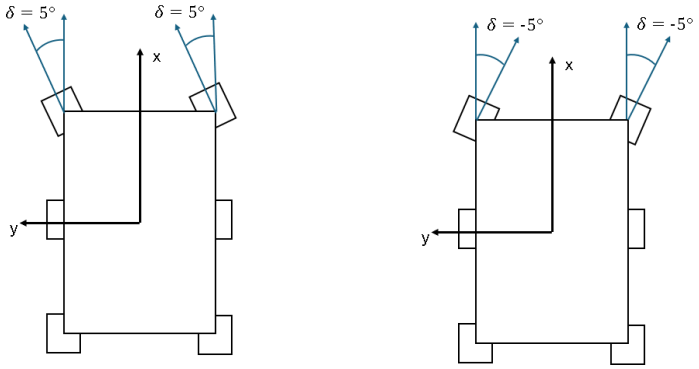

(a) Left turn ($\delta = 5°$) **(b)** Right turn ($\delta = -5°$)

Figure 5.15: Schematic representation of the front steering geometry for both maneuvers.

5.3.1 Plane Motion

Trajectory

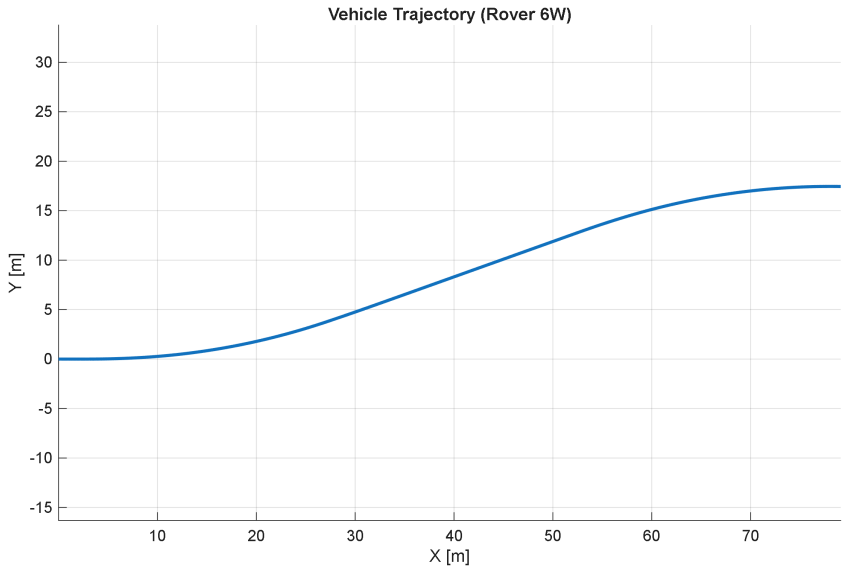

Figure 5.16: Trajectory.

The rover follows a curved trajectory consistent with the imposed steering input.

Golbal reference frame velocities

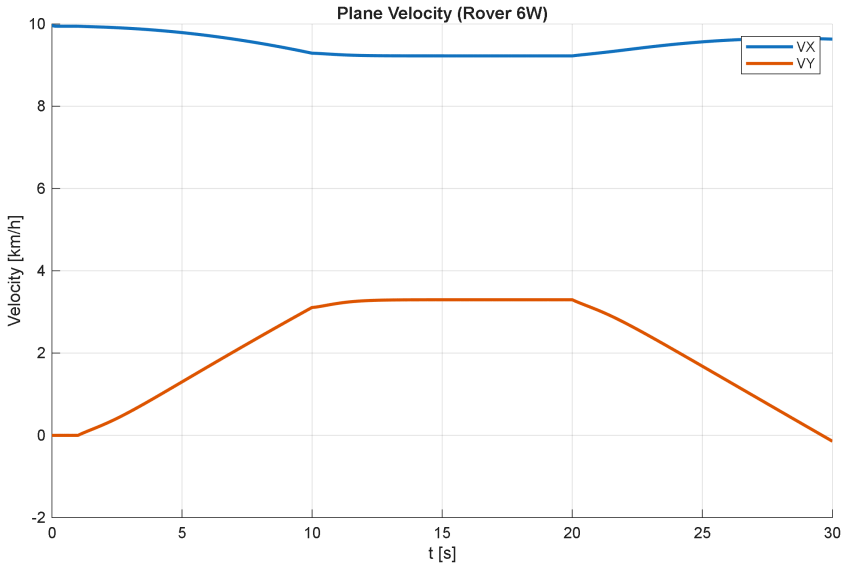

Figure 5.17: Vx vs Vy in global reference frame.

Yaw

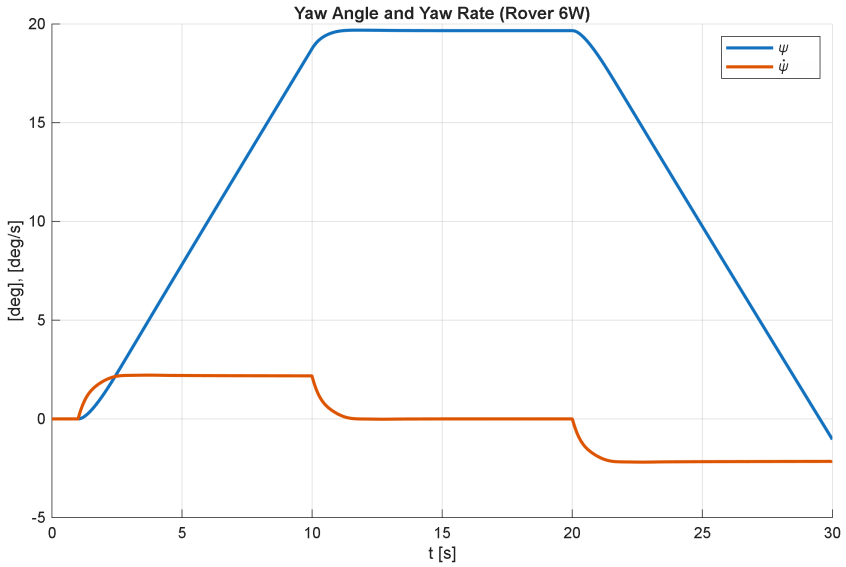

Figure 5.18: Yaw vs Yaw Rate.

The yaw angle and yaw rate are consistent with the resulting vehicle trajectory.

5.3.2 Longitudinal dynamics

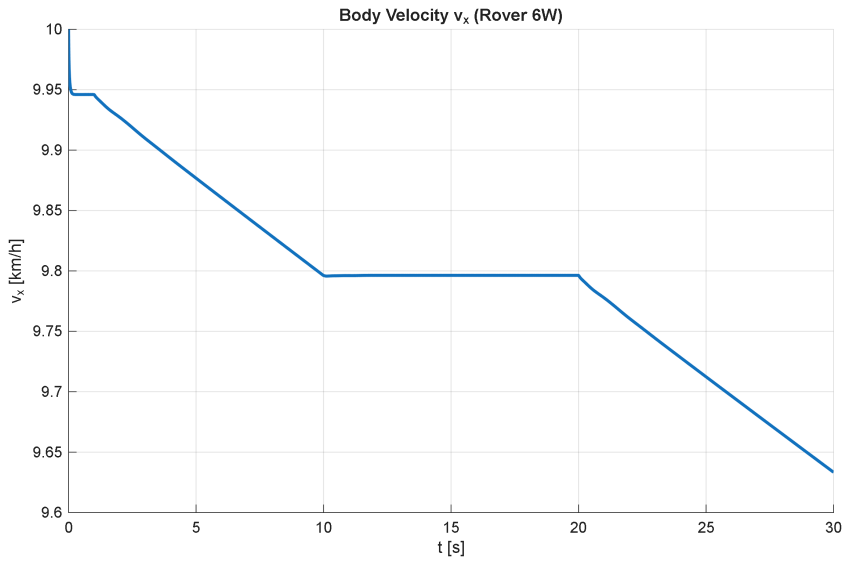

Figure 5.19: Longitudinal velocity vx.

During the steering maneuvers, part of the longitudinal velocity of the vehicle is lost mainly due to the lateral force components generated on the steered wheels, which give a negative component to the longitudinal forces in the vehicle reference frame. It can be observed that the velocity remains constant when the steering input is zero, confirming that the applied torque keeps the vehicle at constant velocity. The initial jump in velocity is due to the imposed initial conditions. At the initial instant the angular velocity imposed on the wheels is $\omega = V_x/r$. However, this condition corresponds to zero slip. Under zero-slip conditions the wheels do not generate tractive forces. Therefore, at the initial instant the only forces acting on the wheels are the motion resistances, which cause a temporary reduction in the vehicle speed. The velocity then stabilizes as the system reaches its equilibrium condition.

5.3.3 Lateral Dynamics

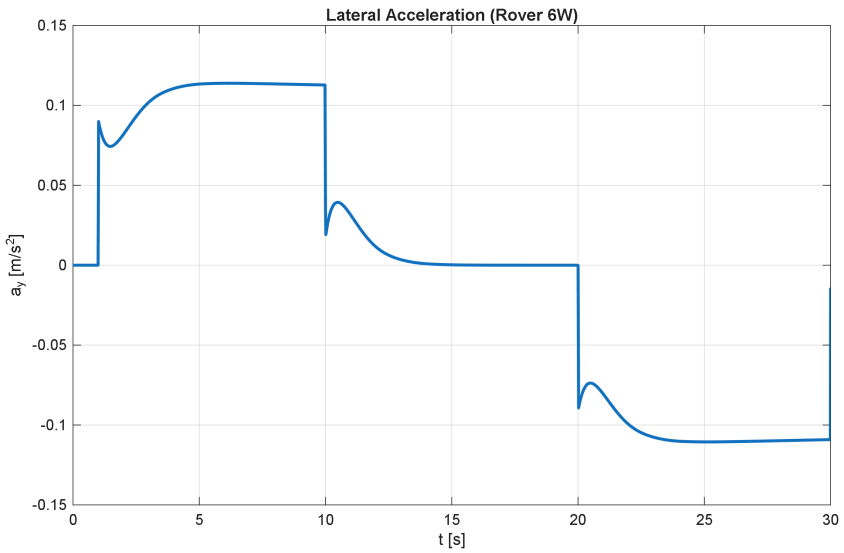

Figure 5.20: Lateral acceleration a_y.

The lateral acceleration is consistent with the vehicle trajectory, initially positive during the left turn, zero during the central phase without steering, and negative during the right turn.

5.3.4 Vehicle Attitude Response

Pitch

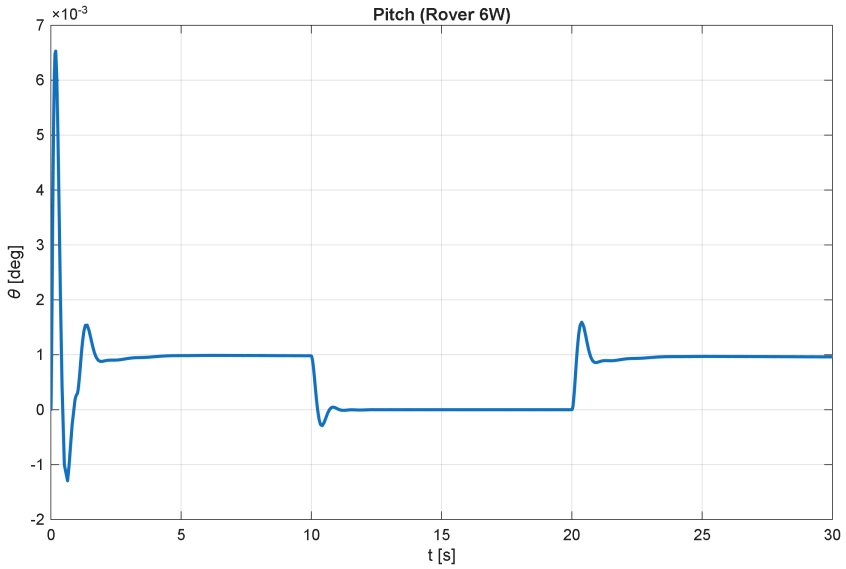

Figure 5.21: Pitch response.

The pitch angle remains generally very small, since the longitudinal acceleration is very low. The initial peak is due to the phenomenon described in the previous section regarding the initial condition of zero slip. The initial deceleration is larger in absolute value than the accelerations generated during the maneuvers.

Roll

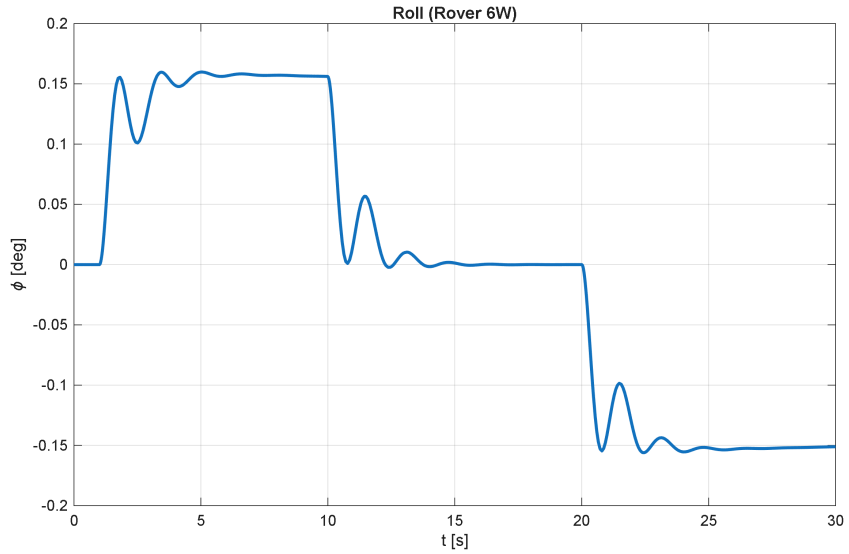

Figure 5.22: Roll response.

The roll motion is consistent with the performed maneuver and with the adopted reference frame. Initially it is positive, indicating that the left side of the vehicle rises. It then becomes zero during the phase without steering and negative during the right turn, indicating that the right side of the vehicle rises.

5.3.5 Wheel-Soil Interaction

Vertical Load

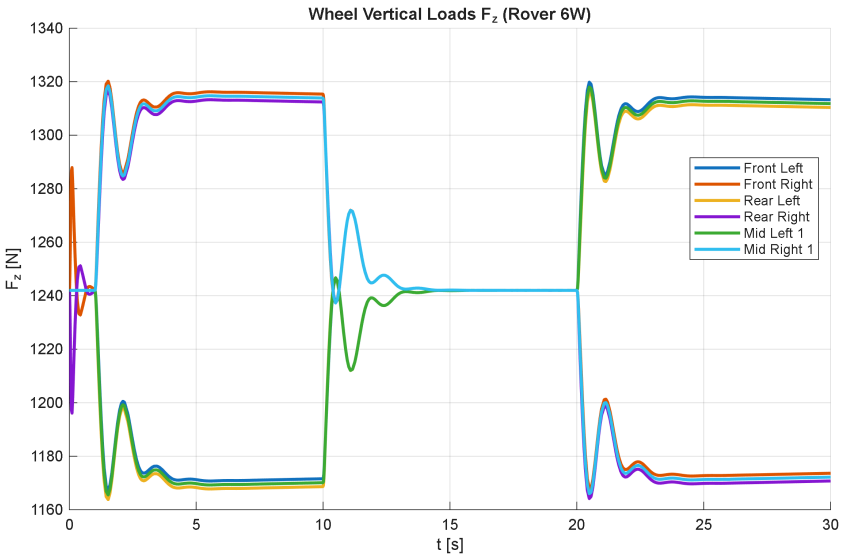

Figure 5.23: Wheel vertical loads.

The distribution of the vertical loads follows the trend of the lateral acceleration. It can be observed that during the left turn the wheels on the left side of the vehicle are more loaded compared to the wheels on the right side. The opposite occurs during the right turn.

Sinkages

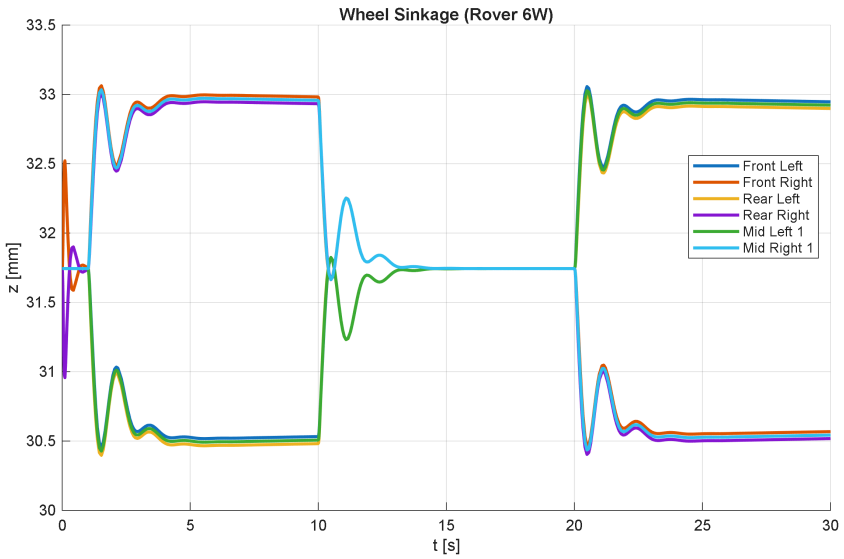

Figure 5.24: Wheel sinkages.

The sinkage follows the trend of the vertical loads acting on the wheels.

Lateral Forces

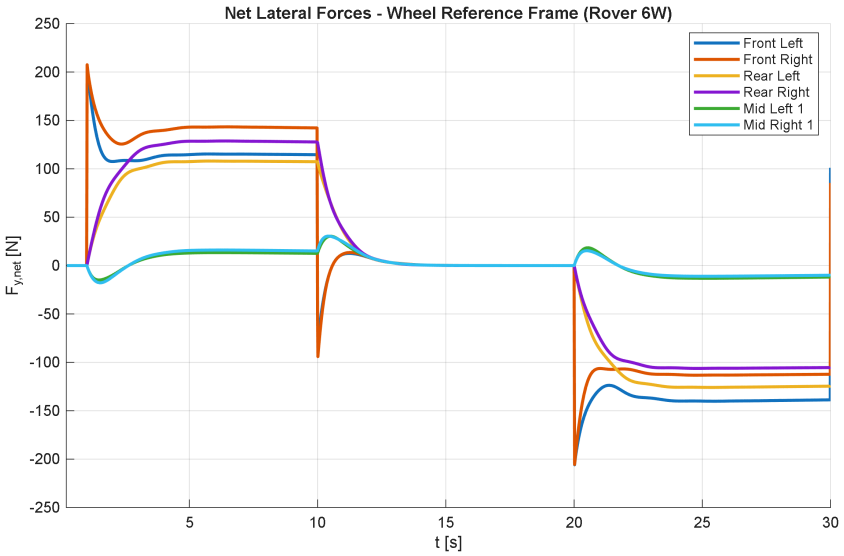

Figure 5.25: Net lateral forces in the wheel reference frames.

Wheel side slip angles

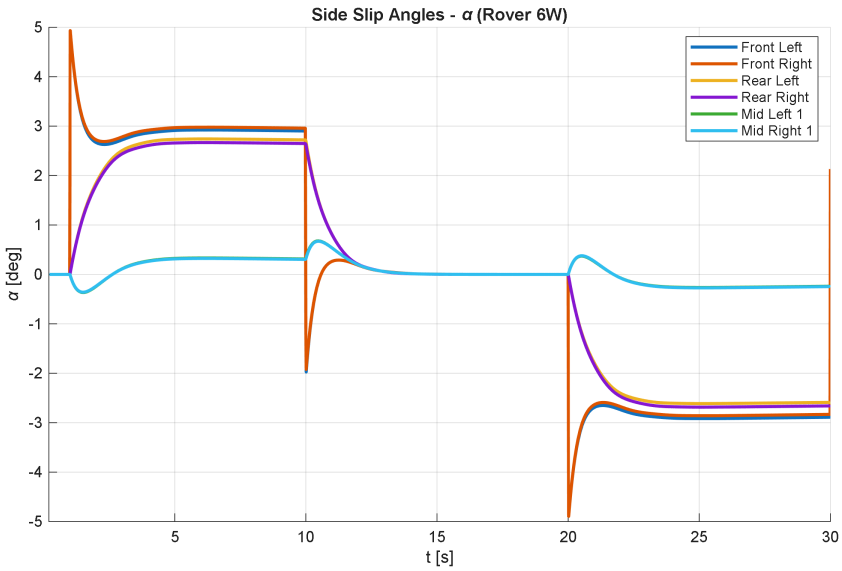

Figure 5.26: Side slip angles.

It can be observed that the lateral forces generated on the wheels follow the trend of the side slip angles. It can be noted that initially the angle on the front wheels is equal to the steering angle δ, and then stabilizes at a constant value during the maneuver.

Wheel angular velocities

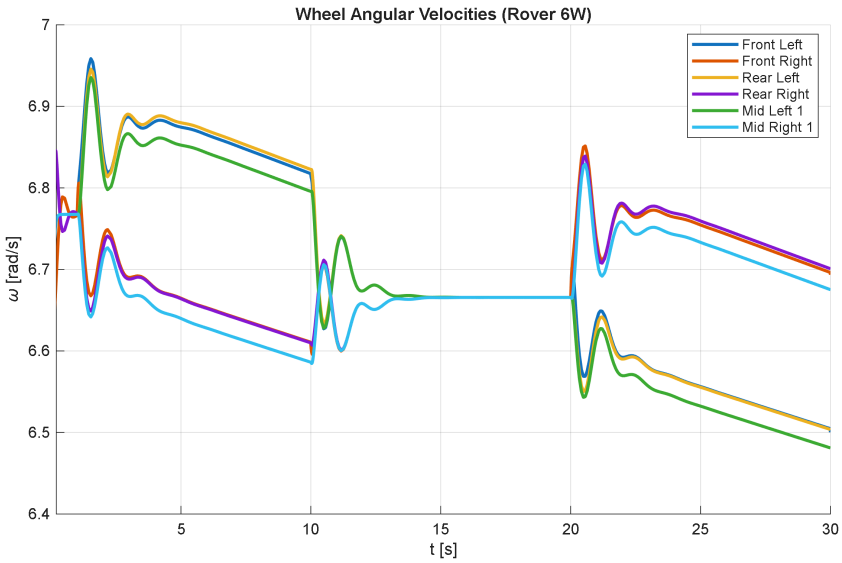

Figure 5.27: Wheel angular velocities.

5.4 Double steer

In this test the same conditions of the previous test are replicated, with the addition of a steering angle also applied to the rear wheels, equal and opposite to that of the front wheels.

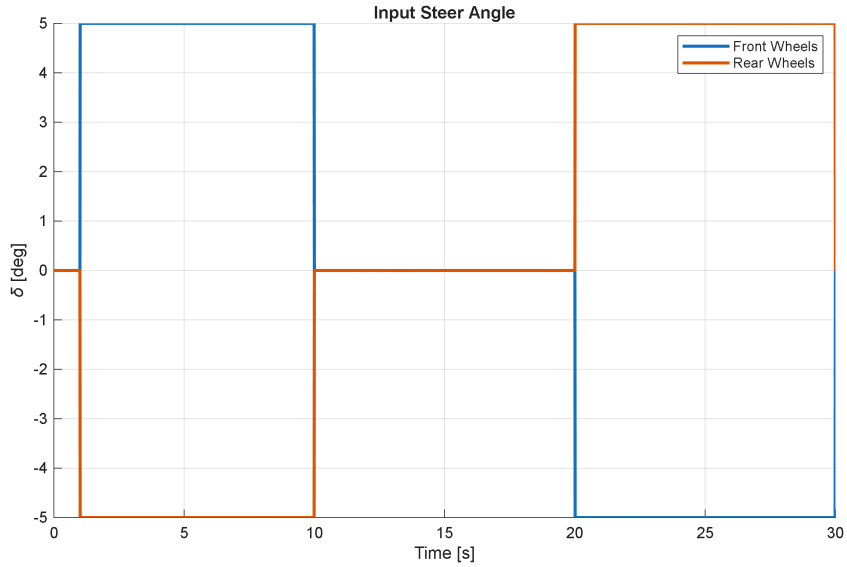

Figure 5.28: Steering input profile δ.

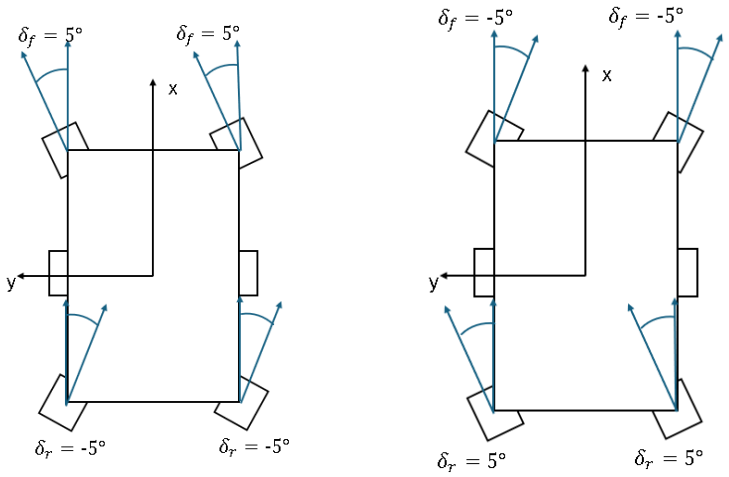

(a) Left turn ($\delta = 5°$) **(b)** Right turn ($\delta = -5°$)

Figure 5.29: Schematic representation of the double steering geometry for both maneuvers.

5.4.1 Plane Motion

Trajectory

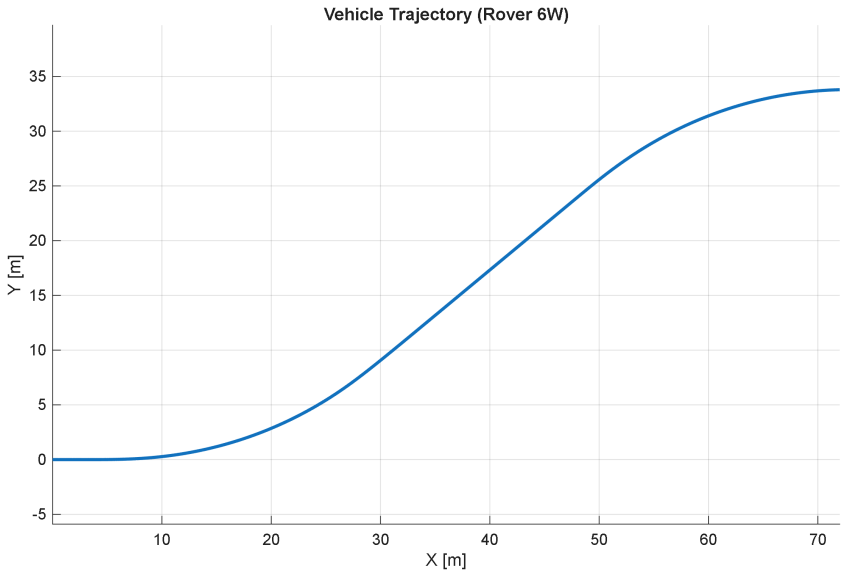

Figure 5.30: Trajectory.

Yaw

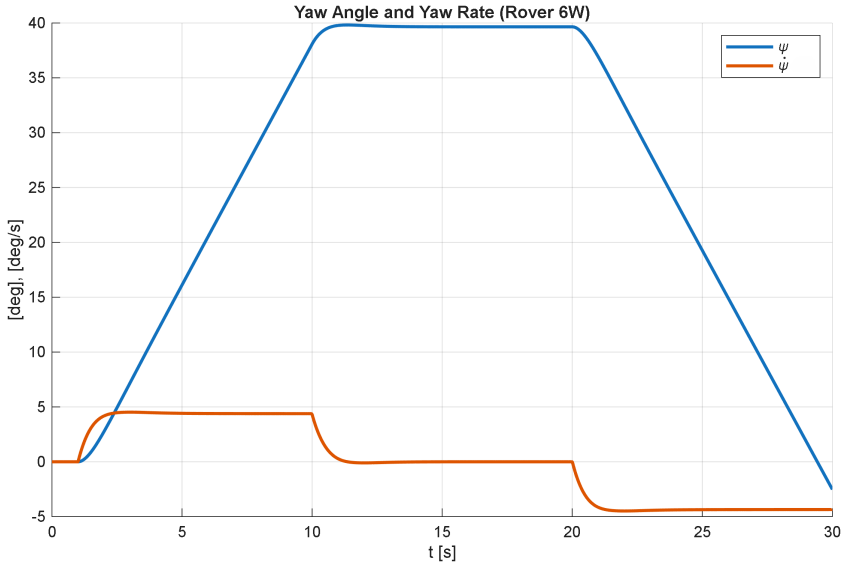

Figure 5.31: Yaw vs Yaw rate.

By comparing with the previous configuration, it can be observed that for the same steering angle the yaw rate is significantly higher in the double steering configuration, resulting in a smaller turning radius and therefore a tighter turn. This behavior is due to the rear lateral forces generated at the steering input. As shown in the plots, these forces are initially negative, following the wheel slip angles α. At the initial input instant, the rear slip angles take the negative value of the steering input because the vehicle has not yet developed a yaw rate to compensate for the kinematics. This initial negative peak creates an additional yaw moment that significantly increases the initial yaw rate, allowing the rover to reach a steady-state turn much faster than a standard steering configuration.

Lateral Forces

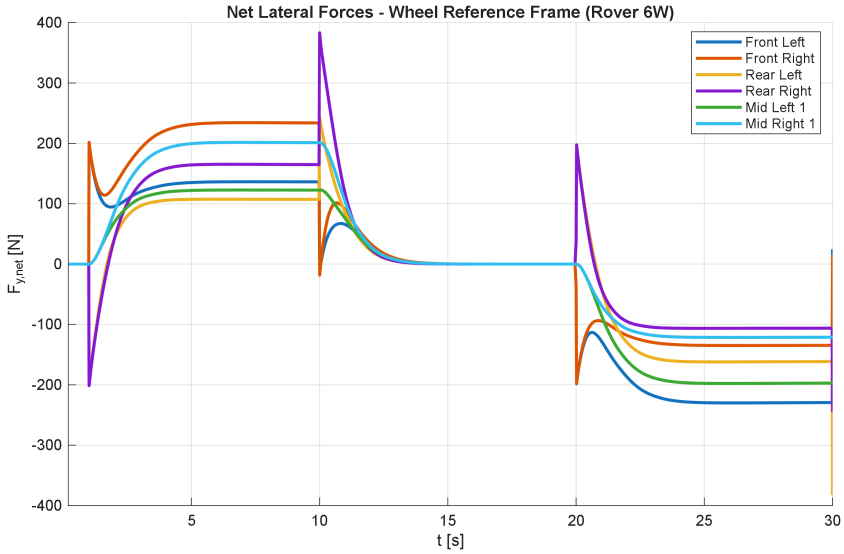

Figure 5.32: Net lateral forces in the wheel reference frames.

5.5 Failure scenario: single motor loss

In this test the response of the system to the failure of a single in-wheel motor is simulated. In particular, all the wheels are subjected to the torque $T = T_{min}$ required to maintain the vehicle at constant velocity, and the torque is removed from the *rear left* wheel. What is expected is that the loss of the motor generates a yaw moment due to the imbalance of forces between the right and left sides of the vehicle.

5.5.1 Planar motion

Trajectory

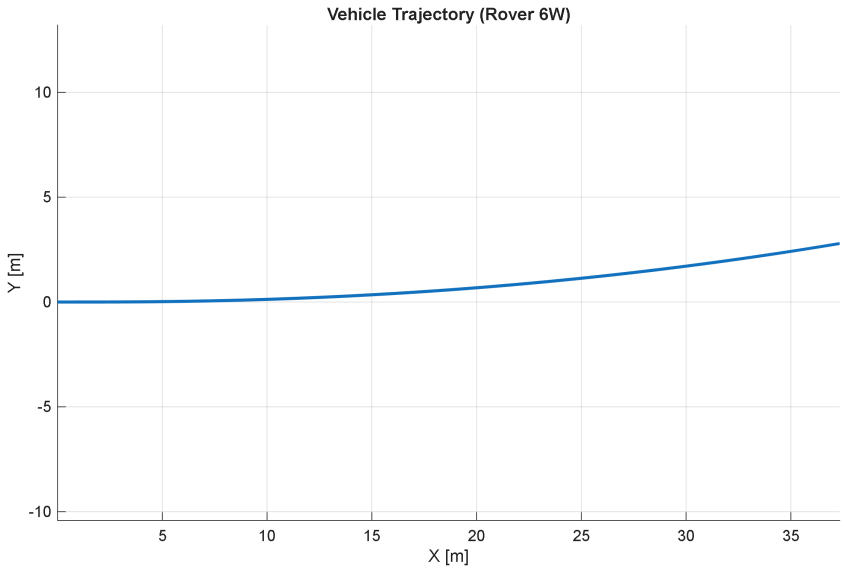

Figure 5.33: Trajectory.

Yaw vs Yaw rate

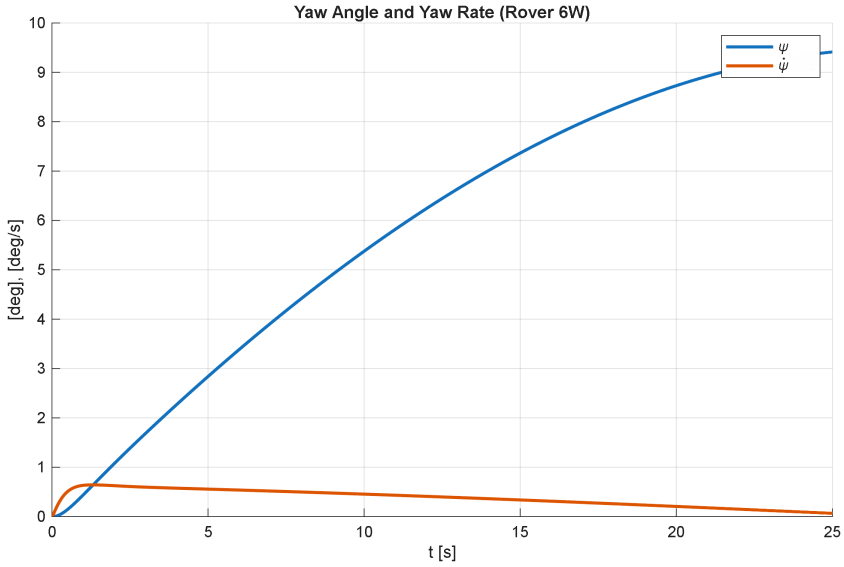

Figure 5.34: Yaw vs Yaw rate.

It can be observed that the imbalance between the forces on the right and left sides produces a yaw moment on the vehicle. This causes the rover to drift from its straight-line path, as the side with the active motors generates more thrust than the side with the failed motor, resulting in an unintended steering effect.

Chapter 6

Conclusion and Future Works

6.1 Discussion of results

From the results obtained in the analyses, it can be observed that the simulator responds coherently to the applied inputs. The dynamic response of the vehicle is consistent with what is expected from the executed maneuvers. Accelerations directly influence the vehicle attitude, inducing roll and pitch motions in accordance with the adopted reference frame. Furthermore, the load transfer caused by the vehicle accelerations directly affects the suspension system, resulting in variations of the vertical loads acting on the wheels. This effect is directly coupled with the terramechanics model. The variation of the vertical load on the wheels directly influences the wheel sinkage into the terrain. The response of the terramechanical model is consistent with the expected physical behavior: both traction and motion resistances increase coherently with the vertical load acting on the wheel. In particular, the vertical load directly affects the traction capability, while it indirectly influences motion resistances through its effect on the sinkage. The modular architecture of the simulator allows the user to compare multiple rover configurations within the same scenario, making it possible to identify the configuration that best satisfies the mission requirements. These results demonstrate that the proposed simulator is capable of capturing the main physical mechanisms governing rover mobility on deformable terrain and can therefore be used as a preliminary design tool for the evaluation of different locomotion architectures.

6.2 Model Limitations

Despite the capabilities of the proposed simulator, several simplifying assumptions have been adopted in the current model. First, the terramechanics formulation relies on simplified analytical models derived from Bekker pressure–sinkage relations and Janosi–Hanamoto shear deformation theory. These models assume a uniform pressure distribution and neglect several complex soil phenomena such as dynamic sinkage and soil compaction history. In addition, the soil model assumes constant terrain properties and does not account for spatial variability of regolith characteristics, which may significantly affect rover mobility on real planetary surfaces. Furthermore, the current implementation does not account for the effect of gravity along sloped terrain. The model assumes a flat surface and therefore neglects the additional gravitational resistance that would arise when the rover operates on inclined slopes. More generally, the terrain is assumed to be perfectly planar and homogeneous. Obstacles, craters, rocks, and other typical irregularities of the lunar terrain are not included in the current model. Consequently, the current model does not investigate the vertical response of the suspension system to terrain irregularities.

6.3 Future developments

In light of what has already been presented both in this chapter and in the previous ones, this section proposes possible future developments for the model.

Wheel Soil Interaction Model

A possible improvement of the simulator concerns the refinement of the wheel–soil interaction model. Future developments could include more advanced terramechanics formulations capable of representing additional physical effects occurring during wheel–terrain interaction that are currently negletcted in the present model.

Active suspension

The current model does not include active or semi-active suspension systems. The suspension units are modeled as purely passive elements characterized by constant stiffness and damping coefficients. The implementation of active suspension control strategies could significantly reduce vehicle oscillations caused by terrain disturbances and aggressive maneuvers. Moreover, the assumption of linear stiffness and damping coefficients may not accurately represent the real behavior of suspension systems under varying operating conditions. Future developments could therefore

include nonlinear suspension models and control algorithms for active vibration mitigation.

Terrain model

Another possible development concerns the representation of the terrain itself. In the current simulator, the terrain is modeled as a perfectly flat surface characterized by constant soil parameters. A more realistic approach would include a three-dimensional terrain model capable of representing slopes, local irregularities, rocks, and craters typically found on the lunar surface. This improvement would allow the study of rover mobility in more realistic mission scenarios and would enable the evaluation of the vehicle's capability to overcome obstacles and operate on uneven terrain.

References

[1] NASA. *First Use of the Lunar Roving Vehicle – July 31, 1971*. 2019. URL: https://www.nasa.gov/image-article/this-week-nasa-history-first-use-of-lunar-roving-vehicle-july-31-1971/ (visited on 02/06/2026) (cit. on pp. 1, 2).

[2] NASA. *New Commercial Artemis Moon Rovers Undergo Testing at NASA*. 2024. URL: https://www.nasa.gov/humans-in-space/new-commercial-artemis-moon-rovers-undergo-testing-at-nasa/ (visited on 02/06/2026) (cit. on p. 1).

[3] M. Bhardwaj, V. Bulsara, D. Kokan, S. Shariff, E. Svarverud, and R. Wirz. *Design of a pressurized lunar rover*. Final Report NASA-CR-192033. Virginia Polytechnic Institute, State University, Department of Aerospace, and Ocean Engineering, Apr. 1992. URL: https://ntrs.nasa.gov/citations/19930008827 (cit. on pp. 2–5).

[4] K. Creel, J. Frampton, D. Honaker, K. McClure, and M. Zeinali. *Pressurized lunar rover*. Senior Design Project Report NASA-CR-192034. Virginia Polytechnic Institute, State University, Department of Aerospace, and Ocean Engineering, May 1992. URL: https://ntrs.nasa.gov/citations/19930008826 (cit. on p. 2).

[5] NASA. *Space Exploration Vehicle (SEV) Rover Concepts*. 2015. URL: https://www.nasa.gov/wp-content/uploads/2015/08/464826main_sev_factsheet_508.pdf?emrc=0855ca (visited on 02/02/2026) (cit. on p. 3).

[6] C. Hirt and W. E. Featherstone. «A 1.5 km-resolution gravity field model of the Moon». In: *Earth and Planetary Science Letters* 329-330 (2012), pp. 22–30. DOI: 10.1016/j.epsl.2012.02.012 (cit. on p. 5).

[7] NASA. *Weather on the Moon*. 2025. URL: https://science.nasa.gov/moon/weather-on-the-moon/ (visited on 11/25/2025) (cit. on p. 5).

[8] V. T. Bickel et al. «Analysis of Lunar Boulder Tracks: Implications for Trafficability of Pyroclastic Deposits». In: *Journal of Geophysical Research: Planets* 124 (2019), pp. 1296–1314. DOI: 10.1029/2018JE005876 (cit. on p. 5).

[9] R. Rajamani. *Vehicle Dynamics and Control*. 2nd ed. Springer, 2012 (cit. on pp. 7, 16, 19).

[10] J. Y. Wong. *Theory of Ground Vehicles*. 3rd ed. John Wiley & Sons, 2001 (cit. on p. 7).

[11] Y. Lim, V. D. Le, and P. A. Bahati. «Development of a New Pressure-Sinkage Model for Rover Wheel-Lunar Soil Interaction based on Dimensional Analysis and Bevameter Tests». In: *Journal of Astronomy and Space Sciences* 38.4 (2021), pp. 237–250. DOI: 10.5140/JASS.2021.38.4.237 (cit. on pp. 21, 22).

[12] Z. Jia, W. Smith, and H. Peng. «Fast Analytical Models of Wheeled Locomotion in Deformable Terrain for Mobile Robots». In: *Robotica* 31 (2012). DOI: 10.1017/S0263574712000069 (cit. on p. 23).

[13] Z. Q. Li and L. K. Bingham. *Terramechanics for LTV Modeling and Simulation*. Tech. rep. (NASA), 2010. URL: https://ntrs.nasa.gov/api/citations/20220010732/downloads/Terramechanics_white_paper.pdf (cit. on pp. 26, 31).

[14] Z. Chi, Y. He, and G. Naterer. «Design Optimization of Vehicle Suspensions with a Quarter-Vehicle Model». In: *Transactions- Canadian Society for Mechanical Engineering* 32 (2008), pp. 297–312. DOI: 10.1139/tcsme-2008-0019 (cit. on p. 48).